Test of nuclear decay rate variation due to an antineutrino flux

Shih-Chieh Liu [1], David Koltick [1,*], Haoyu Wang [1], Jonathan Nistor,[2] Jordan Heim,[2] and Thomas Ward[2]
[1]*Department of Physics and Astronomy, Purdue University, West Lafayette, Indiana 47906, USA*
[2]*TechSource, Inc., Los Alamos, New Mexico 87544, USA*

(Received 12 November 2021; accepted 28 January 2022; published 14 April 2022)

Background: Unexplained variations of the decay rate parameter for weak interaction decays such as $\beta^{\pm}$ decay, electron capture, as well as strong interaction α decay have been reported. Because these variations have been presented by a number of groups, at various locations, using various types of detectors, different isotopes, and over extended periods of time, some researchers have interpreted the source of these variations as not from ambient environmental factors such as temperature, pressure, and humidity but via an unexplained fundamental interaction.

Purpose: The state of decay rate parameter variations experiments is reviewed, and the reported results are placed into a common comparable context by defining a phenomenological cross section. Then we make decay parameter measurements as a function of time at the level of 10^{-5} in the presences of an antineutrino flux with an on-off cycle time of ≈30 days. This level of precision requires a detailed understanding of both systematic and statistical errors; otherwise, systematic errors in the measurement may mimic the decay events of fundamental interactions.

Methods: The experiment searched for variation of the $^{54}_{25}$Mn, e^- capture decay rate parameter and $^{137}_{55}$Cs, β^- decay rate parameter both to a level of precision of 1 part in $\approx 10^5$ by comparing the difference between the decay rate in the presence of an antineutrino flux $\approx 3 \times 10^{12}$ $\overline{\nu}$ cm^{-2} s^{-1} and no flux measurements. The experiment was located 6.53 m from the reactor core of the High Flux Isotope Reactor at the Oak Ridge National Laboratory. Two weak interaction decays, one via electron capture and the other via β^- decay, were selected because the final state and the time reverse state each contain a neutrino and antineutrino, covering arguments that the antineutrino flux may interact differently or not at all in one of the cases.

Results: The γ spectra from both decays were collected and analyzed independently. The measured variation in the decay rate parameters are found to be $\delta\lambda/\lambda = (0.034 \pm 1.38) \times 10^{-5}$ for $^{54}_{25}$Mn and $\delta\lambda/\lambda = (0.67 \pm 1.56) \times 10^{-5}$ for $^{137}_{55}$Cs. These results are consistent with no measurable decay rate parameter variation due to an antineutrino flux, yielding a 68% confidence level upper limit sensitivity for $^{54}_{25}$Mn $\delta\lambda/\lambda \leqslant 1.31 \times 10^{-5}$ or $\sigma \leqslant 1.29 \times 10^{-25}$ cm^2 in cross section and for $^{137}_{55}$Cs $\delta\lambda/\lambda \leqslant 2.23 \times 10^{-5}$ or $\sigma \leqslant 5.69 \times 10^{-27}$ cm^2.

Conclusions: The cross-section upper limit obtained in these null or no observable effect measurements are $\approx 10^4$ times more sensitive than past experiments reporting positive results in ^{54}Mn and ^{137}Cs.

DOI: 10.1103/PhysRevC.105.044610

I. INTRODUCTION

Unexplained variations of the decay rate parameter for weak interaction decays such as $\beta^{\pm}$ decay, and electron capture [1–20], as well as strong interaction α decay [5] have been reported. Because the variation of the decay rate parameter has been presented by a number of groups, located at various locations, using various types of detectors, different isotopes, and over extended periods of time, some researchers have interpreted the source of these variations as not from ambient environmental factors such as temperature, pressure, and humidity but via an unexplained fundamental interaction. Some results show a correlation between an annual periodicity of the decay rate parameter variation, and the variable distance of the Earth from the Sun. The annual variation of the Earth-Sun distance causes a ≈7% variation of the total neutrino flux on the Earth. This flux variation as the source of the decay rate parameter variation is motivated by the large neutrino flux, 6.5×10^{10} ν cm^{-2} s^{-1}, on the Earth dominated by solar fusion. Also, some researchers suggest that decay rate parameters are affected by solar activity such as solar flares [21–24].

However, these conclusions are controversial. This research is focused on the possibilities that the reported variations are an extension of weak interactions. Conventional weak interaction neutrino-nucleon cross sections are 20 orders of magnitude smaller than the reported strong interaction level cross sections being observed in these experiments if caused by neutrinos. The conventional neutrino interaction cross section per nucleon ($\nu + n \rightarrow p^+ + e^-$) is [25]

$$\sigma_{\text{weak}} \approx \frac{4G_F^2 E_\nu^2 (\hbar c)^2}{\pi} \approx 9 \times 10^{-44}\ \text{cm}^2 \left(\frac{E_\nu}{1\ \text{MeV}}\right)^2, \quad (1)$$

*Corresponding author: koltick@purdue.edu

where G_F is the Fermi constant and E_ν is the neutrino energy. Because antineutrinos interact with protons ($\overline{\nu} + p^+ \rightarrow n + e^+$), there is no significant difference between neutrino and antineutrino interaction cross sections on target nuclei. That is, the neutron and proton numbers are similar $\approx A/2$. If a typical neutrino or antineutrino energy is considered to be $\approx$1 MeV, then Eq. (1) leads to a nucleon cross section of

$$\sigma_{\text{weak}} \approx N \times 9 \times 10^{-44}\ \text{cm}^2, \tag{2}$$

where $N \approx A/2$ is the number of neutrons or protons in the nucleus. As will be shown later in Sec. III, the reported decay rate parameter variations are at the level of strong interaction cross sections, not possible conventional weak interaction cross sections.

The goal of this work is to first review the state of decay rate parameter variations experiments and place the reported results into a common comparable context by defining a phenomenological cross section. Then to report on this experiments measurements that maximize the sensitivity to the decay parameter variation caused by a possible extension to the weak interactions. The disadvantage of solar neutrinos as a test source is the low flux variation, $\approx 10^9\ \nu\ \text{cm}^{-2}\ \text{s}^{-1}$, which demands long measurement time. In addition, environmental influences, a source of systematic error, follow this same time cycle. Antineutrinos, on the other hand, can be generated from a nuclear reactor having a stable antineutrino flux ($\approx 3 \times 10^{12}\ \overline{\nu}\ \text{cm}^{-2}\ \text{s}^{-1}$) and much larger flux variations due to the reactor off cycles ($\approx 0\ \nu\ \text{cm}^{-2}\ \text{s}^{-1}$) [26]. For this reason, the experiment was performed at the High Flux Isotope Reactor (HFIR) at the Oak Ridge National Laboratory. The HFIR provides reactor-on and reactor-off cycles of similar duration.

Specifically, our first set of experiments recorded the γ spectra from $^{54}_{25}$Mn electron capture decay,

$$\begin{aligned} {}^{54}_{25}\text{Mn}(3^+) + e^- &\rightarrow {}^{54}_{24}\text{Cr}^*(2^+) + \nu_e \\ &\rightarrow {}^{54}_{24}\text{Cr}(0^+) + \gamma\ (834.8\ \text{keV}). \end{aligned} \tag{3}$$

Even though the weak cross section for ^{54}Mn($Z = 25$) is expected to be at the level of

$$\sigma_{\text{weak}} \approx 2 \times 10^{-42}\ \text{cm}^2, \tag{4}$$

yet while the cross-section sensitivity to decay parameter variation at HFIR is $\approx 10^4$ times more sensitive than the reported positive results, nonetheless this experiment's sensitivity is at strong interaction like cross sections, between 5 and 100 mb. The use of antineutrinos in no way invalidates comparison between this and previous experimental effects based on neutrinos. ^{54}Mn was specially selected because the basic interaction involves a proton ($p^+ + e^- \rightarrow n + \nu$) matching the inverse β^- decay reaction on neutrons caused by antineutrinos.

Similarly, for completeness with a proton in the final state, our second set of experiments recorded the γ spectra from $^{137}_{55}$Cs β^- decay,

$$\begin{aligned} {}^{137}_{55}\text{Cs}(7/2^+) &\rightarrow {}^{137}_{56}\text{Ba}^*(11/2^-) + \beta^- + \bar{\nu}_e \\ &\rightarrow {}^{137}_{56}\text{Ba}(3/2^+) + \gamma\ (661.660\ \text{keV}). \end{aligned} \tag{5}$$

TABLE I. Summary of the ^{32}Si and ^{36}Cl results.

Source	Reference	Sensitivity (size of effect)	Variation
^{32}Si/^{36}Cl	Alburger *et al.*	5×10^{-3}	Positive
^{36}Cl	Kossert *et al.*	4×10^{-4}	Negative
^{32}Si	Semkow *et al.*	1×10^{-3}	Negative

In this case, if weak interactions were to occur involving the neutrons, then the expected cross-section level would be

$$\sigma_{\text{weak}} \approx 7 \times 10^{-42}\ \text{cm}^2. \tag{6}$$

II. HISTORICAL: VARIATION OF RADIOACTIVE DECAY RATE PARAMETERS

Oscillation variations of the radioactive decay rate parameters have been investigated for several decades. A number of groups, such as Alburger, Falkenberg, Veprev, and Jenkins *et al.*, observed time-dependent decay rate parameter variations [1–6,22,24] believed to be not due to variations in ambient environmental factors such as temperature, pressure, and humidity. Some results show a correlation between an annual periodicity of the decay rate parameter and the variable distance of the Earth from the Sun. These results motivate some researchers to conclude that solar neutrino flux variations cause the decay rate parameter variations [4–6,22].

However, the correlation of the radioactive decay rate parameter variation and solar neutrino flux has been challenged by Kossert, Semkow, Meijer, Bruhn, Schrader, and Bellotti *et al.* [8,9,27–31]. These "null evidence" experimental references attribute the decay rate parameter variation to ambient environmental factors or instrumental error instead of the solar neutrino flux variation.

In this section, a summary of some key results will be discussed. The results are sorted by isotopes and date of publishcation. A key comment and a short summary table are presented at the beginning of each discussion. "Positive" represents those observations reporting time-dependent decay rate parameters, whereas "Negative" are those showing no variation results. The size of the observed effect or the experimental sensitivity ($\delta\lambda/\lambda$) in the case of null results are also displayed in the short summary table in each discussion. Table VII and Table VIII display the results of the full literature review and cross-section sensitivities [Eq. (16)] for each reported isotope.

A. ^{32}Si and ^{36}Cl

Alburger *et al.* [1] reported the first observation of decay rate parameter variations in 1986. Alburger worked on the half-life measurement of ^{32}Si with a gas proportional detector over the period 1982 through 1986 at Brookhaven National Laboratory. They unexpectedly observed small periodic annual deviations of the data points from an exponential decay. The authors reported that temperature and humidity "cannot fully account" for observed ratio ^{32}Si /^{36}Cl decay rate variation during their measurement, as shown in Table I. However,

they do not have complete environment records to back up these claims.

Kossert *et al.* [28] reported no decay rate parameter variations of ^{36}Cl measured using a custom-built triple-to-double coincident ratio detector (TDCR) at Physikalisch-Technische Bundesanstalt (PTB). TDCR is an optical chamber with three photomultiplier tubes surrounding a liquid scintillation detector. The sample is placed in the center. A triple coincidence detector is much less sensitive to ambient environmental factors. Kossert measured much smaller variations of ^{36}Cl as shown in Table I than observed by Alburger, but Kossert attributes the small variation to instrumental effects instead of variations of the decay rate parameter. This conclusion is much more reliable than Alburger's because Alburger used a single gas proportional detector which is sensitive to environmental variations.

Semkow [31] has written a review concerning decay rate parameter variations of ^{32}Si from Alburger's results. Semkow explained the variations of ^{32}Si by the change of temperature, causing the air density in the space between the source and the gas proportional detector to change, reducing and increasing the count rate. The higher temperature in the summer causes lower air density in the space between the source and the detector, resulting in less absorption of the lower-energy β particles in the air. Thus, the gas proportional detector collects more β particles at a higher temperature, generating a higher counting rate. The resulting limit is given in Table I.

B. ^{152}Eu, ^{154}Eu, and ^{155}Eu

Siegert *et al.* [32] studied the multi β decay modes of Eu isotopes. Siegert used the strong interaction α-particle ^{226}Ra decay as a reference to determine the half-life of the weak interaction β decays of ^{152}Eu, ^{154}Eu, and ^{155}Eu, measured using two different kinds of detector systems: an ion chamber and a solid-state detector (Ge, Li) at PTB. ^{152}Eu decays to ^{152}Gd by electron capture with 72.1% branching ratio and to ^{152}Sm by β^- decay with branching ratio 27.9%. Siegert reported that the oscillations of ^{226}Ra have a maximum positive deviation in February, and minimum deviation in August. Siegert observed oscillations in ^{226}Ra, as well as in the other isotopes, but explains the effect as follows: "A discharge effect on the charge collecting capacitor, the cables, and the insulator to the ionization chamber electrode caused by background radioactivity such as radon, and daughter products which are known to show seasonal concentration changes."

Siegert concludes the oscillations are proportional to the ionization current. If the oscillations were due to solar neutrinos interacting with isotopes via the weak interactions, then the ^{226}Ra strong interaction decay oscillations should not depend on the ionization current. With these considerations, Siegert's observation are considered to be upper limits, as shown in Table II.

Meijer *et al.* [30] used reactor antineutrinos as a source. Meijer reported null evidence for the decay rate variation of ^{152}Eu using reactor antineutrinos, as shown in Table II. If the solar neutrino variations cause the decay rate parameter variation, then Meijer should have observed a stronger effect compared to Siegert due to the factor-of-10 higher antineutrino flux variation from the reactor cycling. No effect was observed.

TABLE II. Summary of the ^{152}Eu, ^{154}Eu, and ^{155}Eu results.

Source	Reference	Sensitivity	Variation
^{152}Eu, ^{154}Eu, ^{155}Eu	Siegert *et al.*	5×10^{-4}	Negative
^{152}Eu	Meijer *et al.*	1.4×10^{-4}	Negative

C. ^{3}H

Falkenberg [2] is the first one to put forward the hypothesis that the variations of the β decay rate parameters are due to the solar neutrino flux variations. Falkenberg measured the radioactive β decay rate parameter of tritium by a photodiode detector from 1980 to 1982, as shown in Table III. To determine the significance of the data's periodic deviation, the residuals were first fit to a single periodic function. Falkenberg calculated the residuals as the differences between an aperiodic exponential form and the data. Then, he included a cosine function in the fit with a period of 365 days in order to account for the variation away from the aperiodic function. Falkenberg concluded: "There is a positive correlation between the periodically changing solar neutrino flux, and the β decay of tritium."

Bruhn [27] reanalyzed Falkenberg's data and criticized Falkenberg for not making corrections for any background effects in his tritium decay rate measurements. In addition, Bruhn concludes Falkenberg's results are not sufficient for deducing a correlation between the tritium decay rate and the orbital motion of the Earth because neither the period nor amplitude of the deviation coincides with the orbital motion of the Earth. Bruhn concludes: "By taking the deviation of the measurement data with respect to the optimal solution instead of the true solution (in the fits) E.D. Falkenberg cannot separate any (hypothetical) additional background effects in his data from the true solution."

Bruhn's analysis of Falkenberg's data can be used to estimate a limit on the decay parameter variations in ^{3}H. Both results are included in this review, as shown in Table III.

Veprev *et al.* [24] measured the high-energy region of the tritium β-decay spectrum using a liquid scintillation detector system viewed by three photomultipliers. Veprev reported decay rate parameter oscillations which coincide with the solar neutrino flux variation distance from the Earth to the Sun, as shown in Table III. Veprev concludes that the periodicity of the tritium decay rate parameter variations is due to the interactions of the tritium nuclei with solar neutrinos.

TABLE III. Summary of the ^{3}H results.

Source	Reference	Sensitivity (size of effect)	Variation
^{3}H	Falkenberg	3.7×10^{-3}	Positive
^{3}H	Bruhn	2×10^{-3}	Negative
^{3}H	Veprev *et al.*	2×10^{-1}	Positive

TABLE IV. Summary of the ^{54}Mn results.

Source	Reference	Sensitivity (size of effect)	Variation
^{54}Mn	Jenkins *et al.*	1×10^{-3}	Positive
^{54}Mn	Meijer *et al.*	4×10^{-4}	Negative

D. ^{54}Mn

Jenkins *et al.* [6,22] was the first to conclude there is a decay rate parameter variation due to the variable distance of the Earth from the Sun. The results are shown in Table IV. In addition, Jenkins *et al.* reported the detection of a significant decrease in the decay rate parameter of ^{54}Mn during a strong solar flare at the end of 2006. Jenkins measured the count rate of ^{54}Mn and compared it with the solar x-ray data. The deviation is clearly visible on December 12, 2006, through December 17, 2006, which was coincident with a severe solar storm. Jenkins attributed the annual oscillations observed in the data to the variations in solar neutrino flux due to the annual variation in the distance between the Sun and the Earth.

Meijer *et al.* [30] used reactor antineutrinos as a source. Meijer reported null evidence of the ^{54}Mn electron capture decay rate parameter to vary due to an antineutrino flux with improved sensitivity relative to Jenkins's [6,22], as shown in Table IV. The experiments were conducted comparing the γ-ray count rate during reactor on and off periods at an antineutrino flux of $\approx 5 \times 10^{10}\ \bar{\nu}\,\mathrm{cm}^{-2}\,\mathrm{s}^{-1}$. The results showed no variations of the ^{54}Mn decay rate parameter. This challenges Jenkins's conclusions because the solar neutrino flux on the Earth varies only $\approx 7\%$ ($4.6 \times 10^{9}\ \nu\,\mathrm{cm}^{-2}\,\mathrm{s}^{-1}$). Hence, Meijer should have observed an effect more than 10 times larger than that of Jenkins if Jenkins's hypothesis was correct.

E. ^{137}Cs

Schrader *et al.* [8] observed variations in the decay rate measurements of ^{137}Cs using an ionization chamber at PTB. Schrader concludes the small yearly variations are from the measuring electronics, instead of decay rate parameter variations. The results are shown in Table V.

Bellotti *et al.* [33,34] measured the decay rate of ^{137}Cs radioactive source using a NaI scintillation detector and a Ge semiconductor detector. The results are shown in Table V. No significant yearly deviation from the expectations was measured. In addition, the data exhibited no decay rate parameter variations in the presence of the two solar flares of the year 2011 and 2012.

TABLE V. Summary of the ^{137}Cs results.

Source	Reference	Sensitivity	Variation
^{137}Cs	Schrader	4.6×10^{-4}	Negative
^{137}Cs	Bellotti *et al.*	8.5×10^{-5}	Negative

TABLE VI. Summary of the ^{226}Ra results.

Source	Reference	Sensitivity (size of effect)	Variation
^{226}Ra	Siegert *et al.*	1×10^{-3}	Negative
^{226}Ra	Jenkins *et al.*	2×10^{-3}	Positive
^{226}Ra	Bellotti *et al.*	5×10^{-5}	Negative

F. ^{226}Ra

Siegert *et al.* [32] used ^{226}Ra, having a strong interaction α particle decay, to study decay parameter variations. Siegert measured ^{226}Ra decay rate with an ionization chamber at the PTB. Siegert reported that the oscillations of ^{226}Ra have a maximum positive deviation in February and minimum deviation in August. He accounted for these oscillations as due to seasonal environmental variations. This conclusion meets the expectation of a null result if extensions to weak interactions were the source of parameter variations. The results are shown in Table VI.

Jenkins [5] reanalyzed Siegert's ^{226}Ra decay rate data and showed that the observed variations have a correlation to the inverse squared distance between the Earth and the Sun. The results are shown in Table VI. Bellotti *et al.* [35] monitored a ^{226}Ra source for 1 year, using a NaI detector located in the underground Gran Sasso Laboratory. The source was analyzed using Fourier transforms of the residuals for periods from 1 to 100 days and a χ^2 analysis for longer periods. There were no time-dependent statistically significant variations found in the decay constant. In addition, two strong X-class solar flares took place during data collection and, again, no significant evidence of time dependence in the decay constant was observed. The results for the 1-year variation limit is shown in Table VI.

G. Summary of the literature

The literature does not report a consistent picture of decay rate parameter variations. Most of the references have used the Sun as a source of the rate variation through neutrino interactions. However, there is no discussion relating the reported effect or null effect in terms of a cross-section sensitivity. For this reason, the results are not directly comparable, one to another, without such a framework. All authors except one report only the size of the effect relative to the decay rate. This work attempts to place previous results into a unified framework expressed as an interaction cross section due to the neutrino or antineutrino flux observed in the experiment. Furthermore, cross-section sensitivity provides an opportunity to examine further how to proceed in studies of possible decay rate parameter variations of radioactive isotopes.

III. CROSS-SECTION SENSITIVITY TO VARIATIONS OF DECAY RATE PARAMETER

To accomplish a unified frame work the induced decay rate parameter variation is framed in terms of a cross section. The

standard decay rate is given by

$$R(t) = N_0\lambda \exp(-\lambda t) = \frac{N_0}{\tau}\exp\left(\frac{-t}{\tau}\right), \tag{7}$$

where N_0 is the constant of integration which gives the original number of nuclei present when exposure begins. λ is the decay constant, and τ is the mean lifetime which also equals $1/\lambda$. The variation of the radioactive decay rate parameter at time t results in

$$R'(t) = \frac{N_0}{\tau+\delta\tau}\exp\left(\frac{-t}{\tau+\delta\tau}\right), \tag{8}$$

where $\delta\tau$ is the measured variation. The experimental cross section expresses the reaction rate to the exposure from the source and can be written as the (reaction events per unit time per nucleus) divided by the (incident flux of neutrinos per unit area per unit time).

This is equivalent to

$$\sigma = \left|\frac{\delta R(t)}{N(t)}\right| \times \frac{1}{\Delta F_{\nu \text{or} \bar{\nu}}} = \frac{|\delta R(t)/R(t)|}{\tau \times \Delta F_{\nu \text{or} \bar{\nu}}}, \tag{9}$$

where $\delta R(t) = R(t) - R'(t)$ is the number of events that have interacted with the neutrino flux per unit time. $N(t)$ is the number of nuclei at time t. $\Delta F_{\nu \text{or} \bar{\nu}}$ is the variation of the neutrino or antineutrino flux. In addition the definition, $N(t) = R(t)/\lambda$ has been used.

To convert $|\delta R(t)/N(t)|$ into the measuring limit $\delta\lambda/\lambda$, the reaction rate per unit time per nucleus is given by

$$\begin{aligned}\frac{\delta R(t)}{N(t)} &= \frac{R(t) - R'(t)}{N(t)} = \frac{N_0\{\tau^{-1}\exp(-t/\tau) - (\tau+\delta\tau)^{-1}\exp[-t/(\tau+\delta\tau)]\}}{N_o \exp(-t/\tau)} \\ &= \frac{1}{\tau} - \frac{1}{(\tau+\delta\tau)}\exp\left(\frac{-t}{\tau+\delta\tau}\right)\exp\left(\frac{t}{\tau}\right).\end{aligned} \tag{10}$$

Because $\delta\tau \ll \tau$,

$$\begin{aligned}\exp\left(\frac{-t}{\tau+\delta\tau}\right) &\approx \exp\left[-\frac{t}{\tau}\left(1-\frac{\delta\tau}{\tau}\right)\right] \\ &= \exp\left(-\frac{t}{\tau}\right)\exp\left(\frac{\delta\tau}{\tau}\frac{t}{\tau}\right).\end{aligned} \tag{11}$$

Using these approximations in Eq. (10) results in

$$\frac{\delta R(t)}{N(t)} = \frac{1}{\tau}\left[1 - \left(1+\frac{\delta\tau}{\tau}\right)^{-1}\exp\left(\frac{\delta\tau}{\tau}\frac{t}{\tau}\right)\right]. \tag{12}$$

Even with significant decay ($t \approx \tau$), the exponential term in Eq. (12) is still small because $\delta\tau/\tau$ ranges from 10^{-2} to 10^{-5}. From this consideration

$$\begin{aligned}\frac{\delta R(t)}{N(t)} &= \frac{1}{\tau}\left[1 - \left(1-\frac{\delta\tau}{\tau}\right)\left(1+\frac{\delta\tau}{\tau}\frac{t}{\tau}\right)\right] \\ &= \frac{1}{\tau}\left[\frac{\delta\tau}{\tau}\left(1 - \frac{t}{\tau} + \frac{\delta\tau}{\tau}\frac{t}{\tau}\right)\right].\end{aligned} \tag{13}$$

In this experiment as well as all those reviewed the measurement time $t \ll \tau$, therefore,

$$\frac{\delta R(t)}{N(t)} \approx \frac{1}{\tau}\frac{\delta\tau}{\tau}. \tag{14}$$

All the reviewed results as well as this experiment can be framed as a cross section for comparison by dividing by the neutrino flux variation. Inputting the variation decay rate, Eq. (14) into Eq. (9) yields

$$\sigma = \frac{|\delta\tau/\tau|}{\tau \times \Delta F_{\nu \text{or} \bar{\nu}}}, \tag{15}$$

where $\Delta F_{\nu \text{or} \bar{\nu}}$ is the variation of the neutrino or antineutrino flux. With $\delta\tau = -\delta\lambda/\lambda^2$, and $\tau = 1/\lambda$, Eq. (15) can be written

$$\sigma = \frac{|\delta\lambda/\lambda|}{\tau \times \Delta F_{\nu \text{or} \bar{\nu}}}. \tag{16}$$

Using this framework, a cross section or cross-section sensitivity limit can be assigned to each experiment reported in the literature. In addition, two routes to improve the cross-section sensitivity for a given isotope are presented. The first is to measure the isotope decay parameter, $|\delta\lambda/\lambda|$, as precisely as possible. The second is to get as close as possible to the reactor core to increase the on/off antineutrino flux variation, $\Delta F_{\nu \text{or} \bar{\nu}}$. This experiment has taken both approaches.

IV. SOLAR NEUTRINO FLUX

Again, while the source of the reported rate variations in not known, if solar in origin, then it is reasonable to assume it is proportional to the solar neutron flux. As is well known, the source of solar neutrino production is the fusion reaction of hydrogen into helium, resulting in $2\nu_e$ produced by the end of the process. The result is a total solar neutrino flux on the Earth of 6.5×10^{10} cm^{-2} s^{-1}, assuming no ν_e oscillations [39]. Also well known is the Davis result [40] and others [41–44], indicating that $\approx 1/2$ of these solar neutrinos have oscillated before reaching the Earth. However, for the purpose of comparison, the total solar neutrino flux on the Earth in this paper is taken to be 6.5×10^{10} ν cm^{-2} s^{-1}.

As shown, it is the variation in the solar flux that causes the observable decay rate parameter variation not the flux. Due to the Earth's elliptical orbit, with perihelion at 147.1 Mkm and aphelion at 152.1 Mkm and having a semimajor axis of 149.6 Mkm, the solar neutrino flux variation is $\approx 7\%$ found by

$$\frac{r^{-2}_{\text{perihelion}} - r^{-2}_{\text{aphelion}}}{r^{-2}_{\text{semi-major}}} = \frac{(147.1)^{-2} - (152.1)^{-2}}{(149.6)^{-2}}. \tag{17}$$

Thus, the amplitude of the variation of the solar neutrino flux is $\approx 4.6 \times 10^9$ ν cm^{-2} s^{-1} on the Earth.

With this framework, the results in the literature can be compared and are displayed in Table VII and Table VIII.

TABLE VII. Summary of experiments that conclude time dependence of radioactive decay rate parameters. Estimation of the interaction cross section is based on Eq. (16) by inputting the associated size of effect, mean lifetime, as well as neutrino or antineutrino flux from each reference. The variation of the solar neutrino flux is taken to be $4.6 \times 10^9\ \nu\,\mathrm{cm}^{-2}\,\mathrm{s}^{-1}$ on the Earth.

Source	Reference	Mode	Detector type	Measured radiation	Size of effect	ν or $\overline{\nu}$ Variations ($\mathrm{cm}^{-2}\,\mathrm{s}^{-1}$)	Cross section sensitivity (cm^2)
^{3}H	Falkenberg (2001) [3]	β^-	Photodiodes	β^-	3.7×10^{-3}	4.6×10^{9}	1.4×10^{-21}
^{3}H	Veprev (2012) [24]	β^-	Liq. scintillation	β^-	2.0×10^{-1}	4.6×10^{9}	7.8×10^{-20}
^{22}Na/^{44}Ti	O'Keefe (2013) [7]	β^+, ϵ	Solid state (Ge)	γ	3.4×10^{-4}	4.6×10^{9}	6.3×10^{-22}
^{32}Si/^{36}Cl	Alburger (1986) [1]	β^-	Gas proportional	β^-	5.0×10^{-3}	4.6×10^{9}	1.6×10^{-22}
^{36}Cl	Jenkins (2012) [6]	β^-	Geiger-Müller	β^-	1.5×10^{-2}	4.6×10^{9}	2.4×10^{-25}
^{54}Mn	Jenkins (2009) [22]	ϵ	Scintillation	γ	1.0×10^{-3}	4.6×10^{9}	5.6×10^{-21}
^{60}Co	Parkhomov (2005) [18]	β^-	Geiger-Müller	β^-, γ	3.0×10^{-3}	4.6×10^{9}	2.7×10^{-21}
^{60}Co	Baurov (2007) [19]	β^-	Scintillation	γ	7.0×10^{-3}	4.6×10^{9}	6.4×10^{-21}
^{90}Sr/^{90}Y	Parkhomov (2011) [20]	β^-	Geiger-Müller	β^-	2.3×10^{-3}	4.6×10^{9}	3.8×10^{-22}
^{90}Sr/^{90}Y	Sturrock (2012) [15]	β^-	Geiger-Müller	β^-	2.3×10^{-3}	4.6×10^{9}	3.8×10^{-22}
^{90}Sr/^{90}Y	Sturrock (2016) [17]	β^-	Liq. scintillation (TDCR)	β^-	2.0×10^{-4}	4.6×10^{9}	3.3×10^{-23}
^{137}Cs	Baurov (2007) [19]	β^-	Scintillation	γ	2.0×10^{-3}	4.6×10^{9}	3.2×10^{-22}
^{226}Ra	Jenkins (2009) [5]	α	Ion chamber	α	2.0×10^{-3}	4.6×10^{9}	6.0×10^{-24}

TABLE VIII. Summary of experiments that conclude *null* evidence for radioactive decay rate parameter variation. Estimation of the interaction cross section is based on Eq. (16) by inputting the associated size of the effect, mean lifetime, as well as neutrino or antineutrino flux from each reference. The variation of the solar neutrino flux is taken to be $4.6 \times 10^9\ \nu\,\mathrm{cm}^{-2}\,\mathrm{s}^{-1}$ on the Earth. * indicates the reactor antineutrino flux at various locations.

Source	Reference	Mode	Detector type	Measured radiation	Sensitivity	ν or $\overline{\nu}$ Variations ($\mathrm{cm}^{-2}\,\mathrm{s}^{-1}$)	Cross section sensitivity (cm^2)
^{3}H	Bruhn (2002) [27]	β^-	Photodiode	β^-	2.0×10^{-3}	4.6×10^{9}	7.8×10^{-22}
^{22}Na/^{44}Ti	Norman (2009) [36]	β^+, ϵ	Solid state (Ge)	γ	1.8×10^{-3}	4.6×10^{9}	3.2×10^{-21}
^{22}Na	Meijer (2011) [30]	β^+	Solid state (Ge)	γ	2.0×10^{-4}	$^{*}5.0\times10^{10}$	3.4×10^{-23}
^{22}Na	Meijer (2014) [37]	β^+	Solid state (Ge)	γ	5.1×10^{-5}	$^{*}1.6\times10^{13}$	2.7×10^{-26}
^{32}Si/^{36}Cl	Semkow (2009) [31]	β^-	Gas proportional	β^-	1.5×10^{-3}	4.6×10^{9}	4.7×10^{-23}
^{36}Cl	Kossert (2014) [28]	β^-	Liq. scintillation (TDCR)	β^-	4.0×10^{-4}	4.6×10^{9}	6.4×10^{-27}
^{40}K	Bellotti (2018) [35]	ϵ	Scintillation (NaI)	γ	1.0×10^{-5}	4.6×10^{9}	4.0×10^{-32}
^{54}Mn	Meijer (2011) [30]	ϵ	Solid State (Ge)	γ	4.0×10^{-4}	$^{*}5.0\times10^{10}$	2.1×10^{-22}
^{90}Sr/^{90}Y	Kossert (2015) [29]	β^-	Liq. scintillation (TDCR)	β^-	3.0×10^{-4}	4.6×10^{9}	5.0×10^{-23}
^{85}Kr	Schrader (2010) [8]	β^-	Ion chamber	γ	5.0×10^{-4}	4.6×10^{9}	2.2×10^{-22}
^{108m}Ag	Schrader (2010) [8]	ϵ	Ion chamber	γ	9.0×10^{-3}	4.6×10^{9}	9.9×10^{-23}
^{133}Ba	Schrader (2010) [8]	β^-	Ion chamber	γ	1.5×10^{-3}	4.6×10^{9}	6.9×10^{-22}
^{133}Ba/^{108}Ag	Norman (2009) [36]	β^-, ϵ	Solid state (Ge)	γ	1.8×10^{-3}	4.6×10^{9}	8.2×10^{-22}
^{137}Cs	Bellotti (2013) [33]	β^-	Scintillation (NaI)	γ	8.5×10^{-5}	4.6×10^{9}	1.4×10^{-23}
^{137}Cs	Schrader (2010) [8]	β^-	Ion chamber	γ	4.6×10^{-4}	4.6×10^{9}	7.4×10^{-23}
^{137}Cs	Meijer (2011) [30]	β^-	Solid state (Ge)	γ	1.7×10^{-4}	$^{*}5.0\times10^{10}$	2.5×10^{-24}
^{152}Eu	Meijer (2011) [30]	β^-, ϵ	Solid state (Ge)	γ	1.4×10^{-4}	$^{*}5.0\times10^{10}$	4.5×10^{-24}
^{152}Eu	Siegert (1998) [32]	β^-, ϵ	Ion chamber	γ	5.0×10^{-4}	4.6×10^{9}	1.8×10^{-22}
^{152}Eu	Siegert (1998) [32]	β^-, ϵ	Solid state (Ge)	γ	3.0×10^{-2}	4.6×10^{9}	1.6×10^{-21}
^{152}Eu	Schrader (2010) [8]	β^-, ϵ	Ion chamber	γ	5.0×10^{-4}	4.6×10^{9}	1.8×10^{-22}
^{154}Eu	Siegert (1998) [32]	β^-, ϵ	Ion chamber	γ	5.0×10^{-4}	4.6×10^{9}	2.8×10^{-22}
^{154}Eu	Siegert (1998) [32]	β^-, ϵ	Solid state (Ge)	γ	3.0×10^{-2}	4.6×10^{9}	1.7×10^{-20}
^{154}Eu	Schrader (2010) [8]	β^-, ϵ	Ion chamber	γ	5.0×10^{-4}	4.6×10^{9}	2.8×10^{-22}
^{155}Eu	Siegert (1998) [32]	β^-	Solid state (Ge)	γ	3.0×10^{-2}	4.6×10^{9}	3.0×10^{-20}
^{226}Ra	Siegert (1998) [32]	α	Ion chamber	α	1.0×10^{-3}	4.6×10^{9}	3.0×10^{-24}
^{226}Ra	Semkow (2009)[31]	α	Ion chamber	α	3.0×10^{-3}	4.6×10^{9}	9.1×10^{-24}
^{226}Ra	Bellotti (2018) [35]	α	Scintillation (NaI)	γ	1.1×10^{-5}	4.6×10^{9}	3.3×10^{-26}
^{232}Th	Bellotti (2013) [33]	α	Scintillation (NaI)	γ	4.0×10^{-5}	4.6×10^{9}	1.4×10^{-32}
^{238}Pu	Cooper (2009)[38]	α	Radioisotope thermoelectric	α	8.4×10^{-5}	4.6×10^{9}	4.6×10^{-24}
^{241}Am/^{121}Sn	Norman (2009)[36]	β^-, α	Solid state (Ge)	β^-, α	1.8×10^{-3}	4.6×10^{9}	1.6×10^{-22}

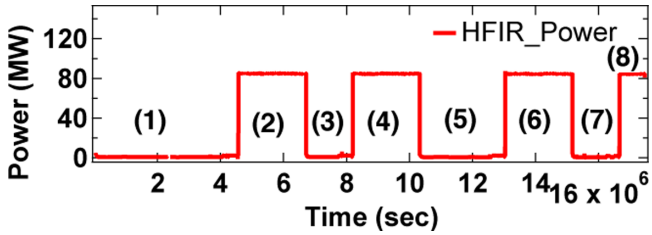

FIG. 1. The HFIR power as a function of time when the ^{54}Mn source was present in the experiment. Each period of the experiment is indicated.

V. THE HIGH FLUX ISOTOPE REACTOR

The antineutrino source for this experiment is the HFIR located at the Oak Ridge National Laboratory. HFIR uses highly enriched ^{235}U as the fuel. The operating cycle consists of full-power operation for approximately 23–27 days using a newly constructed core for each cycle. Figure 1 shows the HFIR reactor power as a function of time during the ^{54}Mn phase of the experiment. The average operating power is calculated from the recorded reactor power data taken every second and is 86.007±0.22 MW. The reactor power is very stable with a variance of $\delta p/p_{\text{mean}} \approx 2.6 \times 10^{-3}$, where δp is the standard deviation of the average power, and p_{mean} is the average power of HFIR in operation.

The average antineutrino flux can be estimated knowing the fissile fuel composition, at HFIR highly enriched ^{235}U, and the reactor's thermal power. The antineutrino production in the core is

$$\frac{dN_{\overline{\nu}}}{dt} = n_{\overline{\nu}} \times \frac{P_H}{E_F}, \tag{18}$$

where P_H is the average thermal power output, E_F is average released thermal energy per fission, and $n_{\overline{\nu}}$ is the average number of antineutrino generated per fission.

Table IX displays the parameters used to find the antineutrino flux for this experiment assuming all the production is from ^{235}U. The thermal energy released per each fission of ^{235}U is

$$\begin{aligned} E_f &= E_F - \langle E_{\overline{\nu}} \rangle \times n_{\overline{\nu}} \\ &= 201.7 - 1.46 \times 5.58 \\ &= 193.6 \text{ MeV}, \end{aligned} \tag{19}$$

where E_F is the released energy per fission and $\langle E_{\overline{\nu}} \rangle$ is the mean energy of the antineutrinos. Hence, the estimated rate,

TABLE IX. Characteristics of antineutrino production from ^{235}U [45].

Type of fuel	^{235}U
Released energy per fission (E_F) (MeV)	201.7
Mean energy of $\overline{\nu}$ ($\langle E_{\overline{\nu}} \rangle$) (MeV)	1.46
Number of $\overline{\nu}$ per fission ($n_{\overline{\nu}}$) ($E > 1.8$ MeV)	5.58

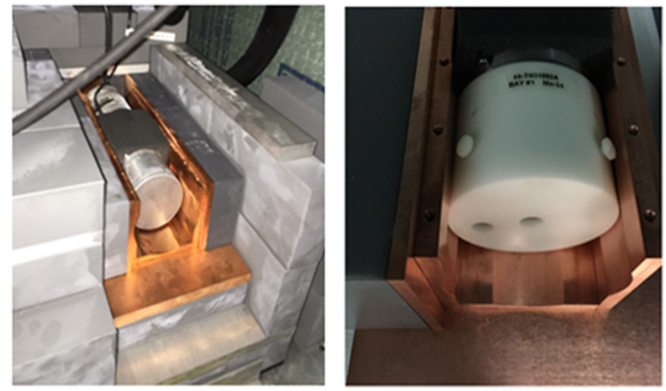

FIG. 2. HPGe configuration. Left: Positioned in the copper florescence shielding without the Source Cup. Right: Source Cup in place. Button source to be place in the center cavity.

$dN_{\overline{\nu}}/dt$, from the HFIR reactor core is given by

$$\frac{dN_{\overline{\nu}}}{dt} = 5.58 \times \frac{86.007 \text{ MW}}{193.6 \text{ MeV}} = 1.53 \times 10^{19}\ \overline{\nu}\,\text{s}^{-1}. \tag{20}$$

The antineutrino flux at the high-purity germanium detector spectrometer (HPGe) detector face, located 6.53 m from the core, is estimated to be $2.86 \times 10^{12}\ \overline{\nu}\,\text{cm}^{-2}\,\text{s}^{-1}$, assuming the core is a point source. This flux is nearly 50 times higher than the solar neutrino flux on the Earth, and the reactors on/off cycles produce more than 600 times larger variation than the solar neutrino flux variation.

VI. EXPERIMENTAL CONFIGURATIONS

The experiment used a 60%, N-type, HPGe system, employing first ^{54}Mn and then $^{137}_{55}$Cs in the same experimental configuration. The ≈1-μCi button sources were held fixed by a polycoarbonate cup on the detectors central axis about 2 cm from the detectors face as shown in Fig. 2. The starting count rate was ≈8 kilo counts per second (kcps). The HPGe energy resolution (full width at half maximum) $\delta E/E = 1.67 \times 10^{-3}$ was measured at $E_\gamma = 1.33$ MeV using a ^{60}Co source.

The shielding house [46] consisted of a 1-inch boronated-polyethylene (b-poly) skin, followed by 4 inches of Pb and an inner liner of 1 inch b-poly. The b-poly served as a neutron shield. The detectors Ge-crystal vacuum housing consisted of an aluminum can with a Be window. Surrounding the vacuum housing was a 5/8-inch-thick copper box to absorb the ≈100-keV Pb fluorescence photons. Additional thin plates of aluminum shielding were placed around the source holder cup to improve the absorption of the ≈10-keV Cu fluorescence photons. Outside the box was an additional 4 inches of Pb shielding for a total of at least 8 inches of Pb shielding surrounding the detector having a total wt. of 5.5 tons. The inner bulk structure is contained within a polystyrene enclosure, whose temperature is maintained by a PID-controlled thermoelectric unit (TECA AHP-1200HC). A set point of 10 °C was chosen for the enclosure based on the enclosures observed nominal equilibrium temperature of 12 °C in the presence of two cold HPGe detectors with their electronic coolers located outside the enclosure. This lower set point has

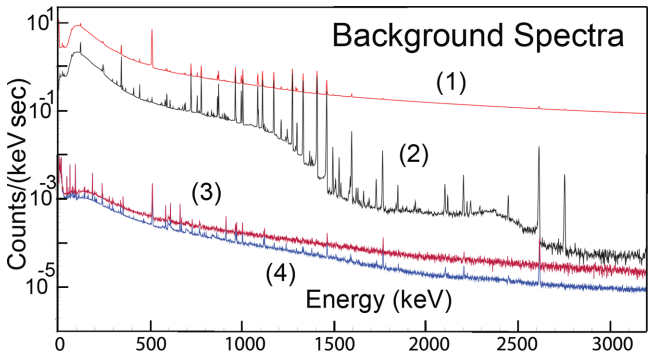

FIG. 3. HFIR background spectra, (1) unshielded reactor on, (2) unshielded reactor off, (3) fully shielded reactor on, and (4) fully shielded reactor off.

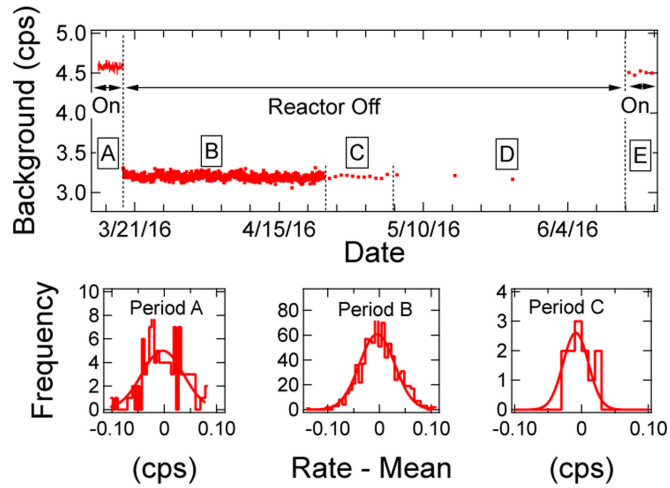

FIG. 4. Top: Full spectrum background rate as a function of time including reactor-on and reactor-off cycles. The source is not present. Left lower: The distribution away from the mean in count rate for 1-h runs during Period A reactor on. Center lower: The distribution away from the mean in count rate for 1-h runs during Period B reactor off. Right lower: The distribution away from the mean in count rate for 1-d runs during Period C reactor off.

the advantage of operating the thermoelectric unit strictly in one mode, cooling mode, for better temperature stability. The enclosure is also continuously purged with nitrogen gas to prevent condensation, which can degrade spectral resolution, and to mitigate influx of contaminants such as ^{226}Ra and ^{41}Ar. System power is routed through uninterruptible power supplies, which provide conditioning as well as approximately 30 minutes of backup power in the event of power loss or necessary platform relocation.

It must be noted that while the detector and source were protected within to the highly controlled shielding house and its environment, the refrigerator, an X-Cooler III, and the electronic spectrometer were mounted on the roof of the shielding house and thus exposed to the reactor building's environmental systems.

VII. SHIELDING PERFORMANCE AND BACKGROUND STABILITY

The background radiation at the experimental location in HFIR is due to (1) the neutrons and γ rays directly produced from the reactor operation, (2) neutron-activated building components, (3) scattered radiation from nearby beamline operations, (4) decay radiation from a nearby source storage room, (5) the shielding materials, (6) natural radioactivity within the building, (7) trace contamination due to the presence of special nuclear material in the building, (8) cosmic radiation, and, finally, (9) the HPGe detector itself. Because the detector is only 6.53 m from the reactor core, γ rays and neutrons produced during reactor on and off periods are significant if the detector were left unshielded. Figure 3 shows the background radiation with and without shielding during reactor-on and -off periods. The spectra show that the shielding is effective in suppressing the backgrounds by a factor greater than 1.8×10^{-4} during reactor-on periods and 6.7×10^{-4} during reactor-off periods.

The reactor on and off background spectra was assumed to be stable over the course of the experiment. To check the time-dependence stability of the background rate, data were collected for nearly 90 days consisting of hourly, daily, and 10-day background runs starting March 9, 2016. The background spectra were collected in the shielding house, which included two reactor-on periods and one reactor-off period. Figure 4 shows the full background spectrum rate as a function of time. Table X summarizes the information during each background collection period. The timing error contribution from the DSPEC-50 are estimated to be below 8.13×10^{-7} cps, which is negligible but tracked throughout the analysis.

The rate distributions for the runs, labeled as Period A, Period B, and Period C, are Gaussian as shown in Fig. 4. The width of the distributions are in agreement with the estimate found using the averaged error of the mean found for each run. As shown in Table X, the statistical mean run error and the width of the run rate distribution are in agreement. This means the calculated errors are correct as proven by the distributions.

The means of three reactor-off Periods B, C, and D are in excellent agreement with their individual variation from the averaged mean shown in the standard deviation row in Table X. These results prove the background is exceptionally stable over the 74-day reactor-off period. All the reactor-off data are used for the background subtraction. The two reactor-on Periods, A and E, are in disagreement at the level of 0.04 ± 0.005 cps from the mean. While the disagreement is small, it is significant. The Period A data were discarded. Just before the background runs were taken the shielding was deconstructed, followed by a week-long period of reconstruction with Period A starting immediately afterwards. This work exposed the shielding to a different and uncontrolled temperature environment. For this reason the first 5 days of data, shown as Period A in Fig. 4, are considered unstable as the detector and shielding system needed time to reach equilibrium. Thus the reactor-on background used for corrections only included Period E, consisting of the average of five 1-d runs.

TABLE X. The average background rate and associated error during the reactor-on or reactor-off periods at HFIR. The distribution error is not available in Periods D and E due to lack of data points. S.D. denotes the standard deviation. The S.D. from the mean is not available for reactor-on Periods A and E because Period A data were dropped from the analysis (see text).

	Period A	Period B	Period C	Period D	Period E
Reactor status	On	Off	Off	Off	On
Duration (d)	5	32	12	30	5
Single run time	1 h	1 h	1 d	10 d	1 d
Timing error (cps)	8.13×10^{-7}	6.77×10^{-7}	2.65×10^{-8}	2.66×10^{-9}	3.00×10^{-8}
Statistical mean run error (cps)	3.57×10^{-2}	2.99×10^{-2}	6.09×10^{-3}	1.93×10^{-3}	7.32×10^{-3}
Distribution error (cps)	3.95×10^{-2}	3.34×10^{-2}	1.80×10^{-2}	N/A	N/A
Mean rate (cps)	4.581±0.004	3.2001±0.001	3.199±0.002	3.201±0.001	4.501±0.003
Reactor-off S.D. from the mean	N/A	0.28	0.63	0.74	N/A
	The average rate in all reactor-off periods:		3.2003 ± 0.0007 cps		
	The average rate in all reactor-on periods:		4.502 ± 0.003 cps		

The average full spectrum rate for the reactor-on background is 4.502 ± 0.003 cps from Period E. The average rate for the reactor-off background is 3.2003 ± 0.0007 cps using Period B, Period C, and Period D, that is, the average of the 74 days of runs.

The full spectrum average rate of ^{54}Mn is ≈6500 cps and ^{137}Cs is ≈8300 cps. From this, the estimated contribution of the reactor-on background spectrum to the overall error is less than $\approx 6 \times 10^{-7}$, and the reactor-off background contribution is less than $\approx 1 \times 10^{-7}$. All are small enough to be neglected but are tracked throughout the analysis.

VIII. DATA COLLECTION

The ^{54}Mn γ spectra were collected from August 14, 2015, at 23:58:22 to March 09, 2016 at 23:12:51 which includes four reactor-off and four reactor-on periods. The total running period consisted of 95 reactor-on days and 114 reactor-off days, totaling over 209 days of data collection. The initial rate was 8.01 kcps with a dead time of ≈13%. The ending data rate was 5.05 kcps with a dead time of ≈8%.

The starting spectrum is shown in Fig. 8. The repetition of the photopeak or pileup peaks are observed with their relative strengths. The strength of the third pileup photopeak relative to the first or true photopeak is $\approx 10^{-6}$.

Similarly, the ^{137}Cs γ spectra were collected from July 03, 2016, at 13:07:37 to November 12, 2016, at 12:16:08, which includes three reactor-off and three reactor-on periods. The total running period consisted of 49 reactor-on days and 84 reactor-off days over 133 days of data collection. The initial rate was 8.30 kcps with a dead time of 13.2%. The ending data rate was 8.23 kcps with a dead time of 13.0%.

For both sources a single spectrum consisted of 24 hours of data collection. The computer clock was continuously synced with stratum 1 public NTP servers via the Meinberg Time Server Monitor software. The software makes corrections to the PC clock gradually, as opposed to immediate "step" corrections. To check the clock offset, between August 14, 2015, and April 10, 2015, a mean value of 0.14 ms and standard deviation of 21 ms was measured. Thus the errors due to timing are negligible, at the level of $\approx 3 \times 10^{-7}$.

IX. DATA ANALYSIS

The goal of the analysis was to achieve a sensitivity at the level of 10^{-5} by keeping the systematic errors small, allowing the statistical error to dominate the measurements. To accomplish this the analysis proceeded as follows: (1) First, each spectrum was independently energy calibrated; (2) using the dead time as reported by the electronic spectrometer, each spectrum is dead-time corrected; and (3) the background spectra are energy matched to the source spectra to account for the difference in calibrations. The background spectrum is next timescaled and amplitude matched and found by comparison to a high-energy region of the source spectrum. Finally, the background is subtracted from the targeted source spectrum. It should be noted that the source spectrum binning width is not adjusted in this process. (4) A deconvolution algorithm is applied in order to find the pile-up free source spectrum. (5) The energy region of interest is defined which forms the signal to be tested for decay rate variations. The region includes the photopeak and other features in order to obtain a semistable signal. (6) Taking advantage of the high-frequency reactor on-off cycles in comparison to the approximate yearly cycle of environmental parameters, a fixed year-long frequency oscillation correction is made, caused by temperature effects on the HPGe refrigerator. (7) Finally a sideband correction is made to correct for nonlinear effects in the energy calibration caused by temperature and humidity effects on the electronic spectrometer housed outside the shielding housing.

X. ENERGY CALIBRATION

To measure the calibration accurately, spectral lines are measured over the full energy range. For background spectra, 13 lines between 3 and 3 MeV were used in the calibration. This assured that the energy region above the third occurrence of the photopeak was well calibrated for the subtraction process. The lines chosen are produced by neutron capture, neutron-induced ambient background, β-decay transitions induced by neutron capture, atomic fluorescence, and natural environmental backgrounds. Because both the ^{54}Mn and ^{137}Cs sources overwhelm these background calibration lines, the source spectra have been calibrated using (1) the indium x-ray,

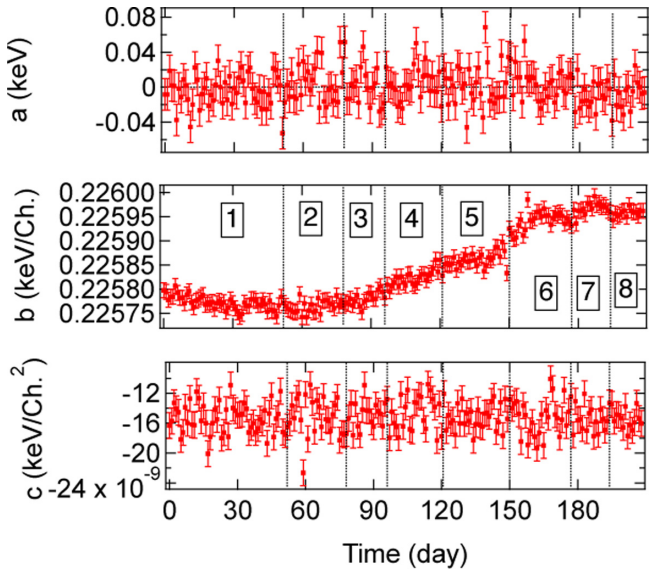

FIG. 5. Nonlinear energy calibration parameters, (top) a_r, (middle) b_r, and (lower) c_r, determined for each of the daily ^{54}Mn spectra. Each period of the experiment is indicated.

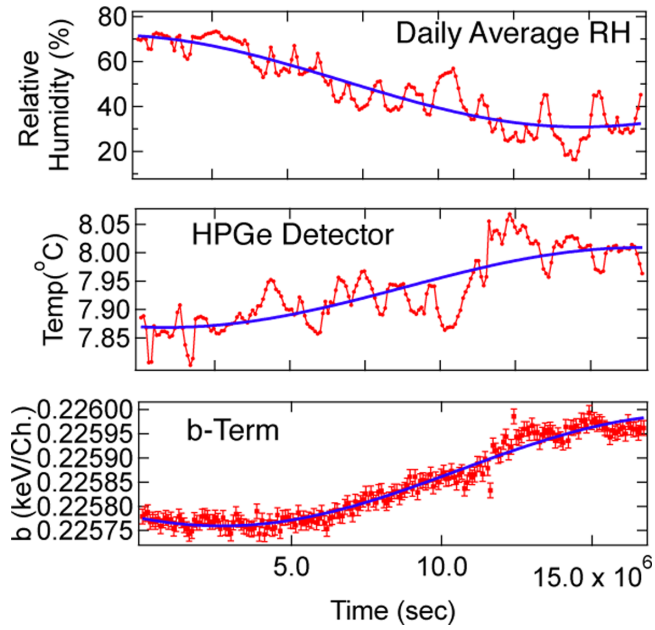

FIG. 6. Daily averages for (upper) the humidity, (middle) surface temperature of the HPGe source detector, and (lower) the linear term b_r. Each is fitted with a periodic function fixed at 1 year, as a function of time.

K-edge peak caused by the source radiation on the indium in the vacuum housing of the HPGe detector; (2) differentiation of the Compton edge; (3) differentiation of the backscattered peak; (4) the sources photopeak; and (5) the ^{208}Tl γ line from natural background. While there are many reoccurrences of these lines as pile-up, their exact energy values were poorly understand, so they could not be used for calibration.

Both source and background spectra calibrations were accomplished using a two-step process. First, a Gaussian lineshape fit was used to find each centroid. Second, the energy calibration was found using a nonlinear three-parameter polynomial fit, weighted by each centroids fitting error. Due to the high statistics in each spectrum, $\approx 10^9$ events, nonlinear fits were required. The resulting χ^2/DoF was improved by a factor of 10 over linear calibration fits.

The exact location of the Compton edge and backscattered peaks are related to the detector, shielding, and source geometry and could not be found by first principles. For this reason a single parameter iterative calibration process was performed on the first day's spectrum of each source, based on minimizing the third-order polynomial fit. Once the energy values were found, all five lines energy values were fixed and used to calibrate all subsequent source spectra.

XI. CALIBRATION COEFFICIENTS

The calibration function is given in Eq. (21). The fitting parameters and their fitting errors as a function of time for the ^{54}Mn runs are displayed in Fig. 5,

$$E = a_r + b_r x + c_r x^2, \tag{21}$$

where a_r, b_r, and c_r are the calibration coefficient of rth daily spectrum and x is the channel number of the spectrum. Each parameter is discussed in turn.

A. Constant terms a_r

The constant terms a_r vary about zero with variance of $\approx$0.02 keV or less than 10% of the 0.225-keV single bin width. The a_r parameters measure offsets in the energy scales. a_r is expected to be nearly zero in a low-noise environment, which is the case in this experiment. The stability of a_r yields a stable region of interest (ROI) containing the photopeak.

B. Linear terms b_r

The linear parameter, b_r, is well measured with an accuracy of $\delta b/b \approx 7 \times 10^{-5}$. Nonetheless, the b_r varies over the course of the experiment due to temperature variations driven by the X-cooler, the HPGe refrigerator, responding to variation in the humidity. To show this, the linear b_r parameters are fit to a periodic function,

$$b(t) = b_0 + A\sin(\omega t + \phi), \tag{22}$$

in which ω is fixed at 1-year. The resulting excellent fit, χ^2/DoF = 1.14, is displayed in Fig. 6, and the phase given in Table XI.

TABLE XI. Comparison of yearly cycling of humidity and temperature for the HPGe source detector and the linear term b values relative to the experiment's starting date.

Fixed $\omega = 1$ year	Negative phase (ϕ)
Out-of-phase humidity	103 ± 1 day
Source detector temperature	101 ± 6 day
Linear term b	122 ± 2 day

Likewise, the detector temperature is fit as a function of time, with the fit shown in Fig. 6 and the resulting phase given in Table XI. It should be noted that the magnitude of b_r is directly related to the detectors band gap which has a temperature dependence given by Varshni's empirical form [47]. Varshni's form predicts that lower temperatures produce larger band gaps and vice versa. Since lower b_r values represent larger band gaps, b and the detector temperature should be in phase. As shown in Table XI, the phases are in reasonable agreement.

While the temperature of the housing enclosure is held at a very stable temperature $10.00 \pm 0.027\,^{\circ}$C, the detector's X-cooler is outside the housing. The X-cooler is affected by the humidity in the following manner: As the humidity increases the heat capacity of the air increases, allowing more efficient cooling, lowering the temperature of the detector, and thus increasing the band gap. Likewise, as the humidity decreases, the heat capacity of the air decreases, yielding less efficient cooling and allowing the detector temperature to increase, narrowing the band gap. In this way, the humidity variation should be out of phase with both the detector temperature and the b_r parameters, as is the case shown in Fig. 6 and Table XI, using the same fixed fit. While these effects are small, they produce yearly oscillations in the data at the level of 10^{-3}.

C. Nonlinear terms c_r

The c_r parameter is the nonlinear term, significant only for high-energy spectral lines. It is due to temperature variations of the DSPEC-50 electronic spectrometer placement outside the temperature-controlled housing. While in the plot c_r appears stable and small, $\approx 10^{-8}$ keV/bin, at large channel number, for example, $\approx$4000 where the ^{54}Mn photopeak is located, it accounts for a shift of one full bin (0.225 keV) in the spectrum.

Finally, these calibration parameters result in a highly stable photopeak energy as a function of the time. The average energy of the ^{54}Mn photopeak is 834.849 ± 0.001 keV, within the uncertainty of the ^{54}Mn standard error value ± 0.003 keV [48]. Likewise, the ^{137}Cs photopeak is highly stable with a mean energy of 661.650 ± 0.011 keV.

XII. CORRECTION PROCEDURES

Because the analysis of the HPGe spectrum requires mathematical manipulation of each channel, statistical and systematic error must be considered channel by channel. There are three significant systematic errors associated with the measurement: (1) the electronic dead time from the DSPEC-50 electronic spectrometer, (2) the neutron and natural background radiation which produces an unwanted background spectrum, and (3) the electronic pile-up due to the inability of the electronics spectrometer to distinguish two or more pulses occurring within a time window smaller than the electronics resolving time.

Each correction will be discussed in order taken; the energy calibration of the background spectra (already discussed); the dead time produced by the digital spectrometer; background spectra rebinning, rescaling, and subtraction; the pile-up correction using a deconvolution algorithm; integration of the ROI for each 24-h data run; a sideband low-frequency oscillation correction; and, finally, the electronics instability correction due to ambient environmental effects.

TABLE XII. Proprieties of the full ^{54}Mn spectrum. The first-day spectrum is in a reactor-off period. The last day is in a reactor-on period.

Full spectrum daily ratio	First day (reactor off)	Last day (reactor on)
Spectrum rate (cps)	8009.5	5054.5
Background (fraction) (cps)	3.1 (0.04%)	4.7 (0.09%)
Pile-up (fraction) (cps)	33.5 (0.4%)	13.7 (0.04%)
Dead time/day (s)	11166.4	7235.9
Pulse generated dead time (μs)	16	16
Double pulse resolution (μs)	0.5	0.5
Background-source pileup (cps)	0.013	0.012

A. Dead-time correction

Dead time is the integration of those periods in which the electronics do not give a response to detector pulses. The electronic spectrometer follows the nonparalyzable model. The DSPEC-50 has two different ways it processes the second incoming pulse from the HPGe detector if the previous pulse has not returned to pole-zero baseline. First, the DSPEC-50 will reject the second pulse if it is recognized. Second, if the second pulse arrives unrecognized, that is, within a shorter time than the electronic resolving time, then the DSPEC-50 records the sum of two pules which is called electronic pile-up. The dead-time correction would account for the total number of counts in the full spectrum if there were no electronic pile-up effects.

There are two types of pile-up effects—low-energy and high-energy pile-up—defined with respect to the ROI region. The DSPEC-50 dead-time correction is only correct when applied to the photopeak counts. However, the analysis is not limited to the photopeak. The dead-time correction does correctly account for the high-energy pile-up, that is the loss of events out of the ROI region. However, the dead-time correction does not take into account the lower-energy pile-up effect, that is, low-energy events combining to an energy that places the combined event into the photopeak ROI. Triple pile-up is also observed at the level of 10^{-6} of the photopeak rate and is neglected in this analysis.

Table XII gives the properties of the ^{54}Mn spectrum using the corrections. While it may appear optimal to finalize the dead-time corrections before moving on to other corrections, this is not possible. The pile-up correction is entangled with other corrections as will be shown. The dead-time correction is accurate to 10^{-3} if pile-up is not taken into account. The pile-up correction can be untangled by first noting in Table XII that the full spectrum background pile-up with the source is only 0.013 cps, calculated using the double pulse time resolution 0.5 μs. This rate is much smaller in the ROI. For this reason, the background-source pile-up is negligible,

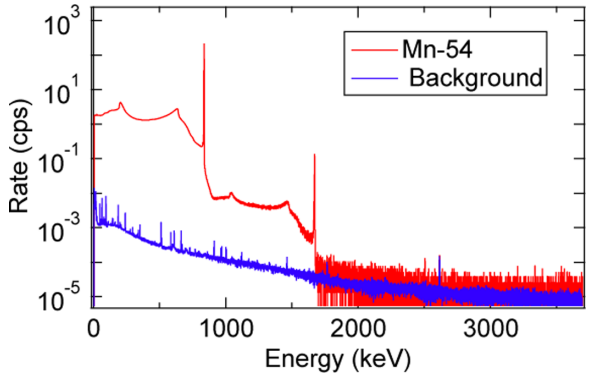

FIG. 7. Logarithmic ($\log_{10}$) scale of the ^{54}Mn γ spectrum before background spectrum subtraction and the background spectrum.

allowing the background to be first subtracted from the dead-time-corrected source spectrum.

B. Background rebinning, rescaling, and subtraction

Background subtraction takes into account that the source spectra and background spectra have been calibrated using different nonlinear calibrations. As with this, and other corrections, the source spectrum is never energy scale altered during corrections. Corrections are always energy matched to the source calibration. In this way, the correction contributes the minimum possible error to the analysis. For this reason, the background correction is a three-step process. (1) The dead-time correction is made channel by channel. (2) Then the background data are energy rescaled to match the difference in energy calibration parameters between the source data and the background data. (3) Finally, the collected background is normalized to the daily rate above the third recursion of the photopeak due to pile-up. This region is unaffected by pile-up. For the ^{54}Mn source this range extends from $E_{\text{low}} = 2515$ keV to $E_{\text{high}} = 3680$ keV. The correction is made using a single scaling parameter by matching the total number of counts in the source spectrum and background histograms in this comparison region. The completion of these correction are intricate and are discussed elsewhere [49]. After completing all the correction to the background, the resulting background spectrum is subtracted from the source spectrum.

Figure 7 compares the first day of the ^{54}Mn spectrum before background correction and the background spectrum after the matching correction. The process is channel-by-channel (bin-by-bin) subtraction using either the reactor-on background or reactor-off background spectra. The ratio of the ^{54}Mn spectrum's error $\sigma(i)_{\text{source}}$ to the error caused by amplitude scaling of the background is

$$\frac{\sigma(i)_{\text{amplitude}}}{\sigma(i)_{\text{source}}} = \begin{Bmatrix} 2 \times 10^{-3} & \text{Compton region} \\ 1 \times 10^{-4} & \text{ROI region} \end{Bmatrix}. \quad (23)$$

The background statistical and rebinning error $\sigma(i)_{\text{background}}$, and the amplitude scaling error $\sigma(i)_{\text{amplitude}}$, are extremely small compared to the statistical error in the ^{54}Mn spectrum and are dropped. The corrected spectrum uncertainty

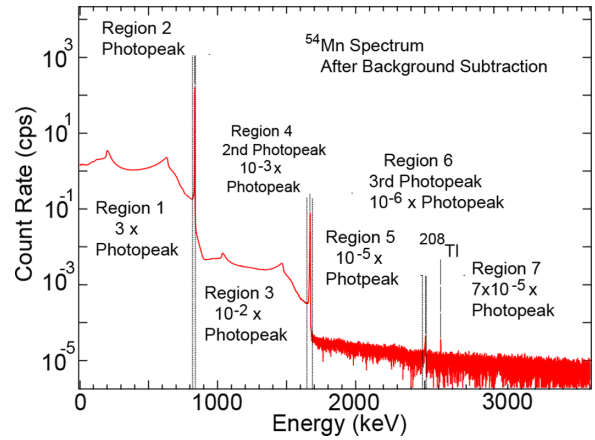

FIG. 8. Logarithmic ($\log_{10}$) scale of the ^{54}Mn γ-ray spectrum after background subtraction. The ^{54}Mn photopeak is at 834.848 keV. The second coincident photopeak is at ≈1665 keV, and the third coincident photopeak is at ≈2497 keV.

$\sigma(i)_{\text{corrected}}$ in the ith bin is

$$\sigma(i)_{\text{corrected}} \approx \sigma(i)_{\text{source}}. \quad (24)$$

Thus, the background subtraction contributes no error to the corrected ^{54}Mn spectrum.

C. Pile-up correction by deconvolution algorithm

With the background correction completed, the pile-up correction can be made. Figure 8 shows the full ^{54}Mn γ-ray spectrum after background subtraction. The ^{54}Mn spectrum consists of a "Compton" region in which the full energy of the γ ray was not completely absorbed. This region is labeled Region 1 in Fig. 8. The full-energy peak, called the photopeak, is produced by the complete absorption of the γ energy, as shown in Region 2. The ratio of events in Region 1 to Region 2 is nearly 3. One of the major systematic error in ^{54}Mn spectrum is the electronic pile-up. The pile-up, shown in Regions 3 and 4, is caused by two independent nuclear decay photons which interact with the detector within a time period shorter than the resolving time of the detector. Because the primary photopeak can be treated as a δ function, the pile-up Regions 3 and 4 appear as an integration of the "Compton" Region 1, with the photopeak, Region 2, yielding a mirrorlike image of the lower-energy single-γ-ray region but at higher energy. Regions 3 and 4 are called the first pile-up of the ^{54}Mn spectrum that has the ratio of 10^{-2} to the first photopeak. Regions 5 and 6 are called the second pile-up of the ^{54}Mn spectrum in which three γ rays interact with the detector in a time shorter than the resolving time. This region has a ratio to the primary photopeak of nearly 10^{-5}. The expected measuring sensitivity in the experiment is to be 1 part in 10^5, so the pile-up corrections play a key role to improve the measuring sensitivity.

To obtain a highly accurate ^{54}Mn spectrum, composed of single events, the piled-up events are removed through an iterative deconvolution algorithm. This procedure is performed for the energy-calibrated spectra and background-subtracted spectra. Each deconvolution cycle starts with only the energy

region containing the photopeak and below. It proceeds by calculating the destination bin of any two events residing in the single-events region. As a metric, the reduced S value [50] of the residuals between the input spectrum to the resulting deconvolution in the first-order pileup region is computed. The deconvolution spectrum is generated in the following way:

$$P_k(E_i + E_j) = \sum_{k=i+j} P_i(E_i)P_j(E_j), \tag{25}$$

where it is assumed that the energy value refers to the bin center. Unfortunately, the energy associated with the convoluted bin k does not match the energy bins associated with the original energy spectrum because of the nonlinear calibration. The deconvolution spectrum must be appropriately energy scaled before it can be subtracted from the original energy spectrum. Thus, the energy scale of the pile-up spectrum must be corrected to match the original spectrum energy scale. Because the energy scale of the ^{54}Mn spectra is nonlinear, it is convenient to match up energy scales directly for this subtraction process. Again, only the pile-up spectrum is manipulated. This procedure is similar to the previous background correction process.

Once the pile-up spectrum is generated and appropriately energy matched to the ^{54}Mn spectrum, the pile-up spectrum is compared with the first pile-up region of the input spectrum for amplitude rescaling. The comparison region for the source, and the pileup spectrum, is the energy region between the end of the primary photopeak (first) and the end of the pileup photopeak (second), which is within the boundaries of Regions 2 to 4 in Fig. 8. A linear regression method with uncertainties in two dimensions is utilized to obtain the scaling factor [50]. After the pile-up spectrum amplitude scaling, the pileup spectrum is subtracted from the original starting energy spectrum that served as the first guess to generate the pileup spectrum. This process is then iterated until the starting spectrum and the generated pileup spectrum stabilize. A reduced S-value test is used to stabilize the pile-up spectrum [50]. Each iteration requires reconstruction of the deconvolution or pileup spectrum to correctly compare it to, and subtract it from, its generating spectrum. The deconvolution algorithm flowchart is shown in Fig. 9. Figure 10 shows the starting spectrum and the resulting pile-up spectrum. As shown the method compares well in the comparison region; however, the pile-up photopeak's width is underestimated because the energy resolution is not a linear function of energy. Nonetheless, this effect does not alter the estimate of the pile-up within the region of the single event spectrum due to its smoothness in this region.

The χ^2_{DoF} of the difference between the convolution and the data in the match region is 1.26 indicating an acceptable convergence. Using the first day's data in which the pileup is largest, the rate difference between the convolution spectrum and the ^{54}Mn spectrum in the match region is $\Delta R = 8 \times 10^{-6}$ cps, again showing an excellent match for the convolution, as the total rate in this region is 15.176 ± 0.014 cps. Because the total rate difference is so much smaller than the regions total rate error, this indicates that the error generated by the convolution method is dominated by the statistics in the ^{54}Mn spectrum.

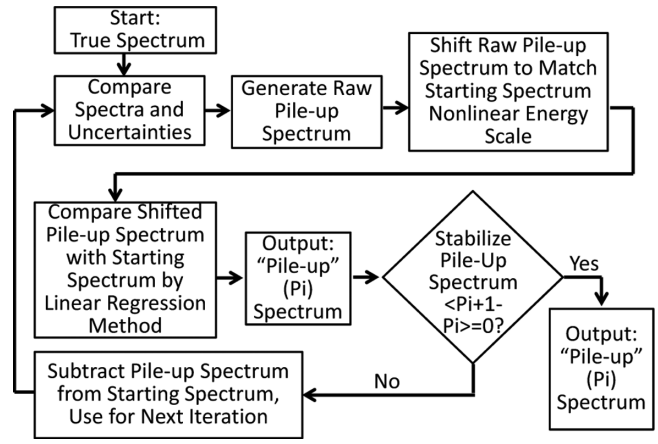

FIG. 9. Deconvolution algorithm used to determine pileup events to be removed from the ^{54}Mn spectrum.

To estimate the error caused by the pileup subtraction, first consider, from above, that the accuracy of the background match region rate is known to be $\approx 10^{-3}$. Assuming a similar background pileup rate in the regions, including and below the ^{54}Mn photopeak, means the pileup correction is at the level of 0.014 cps. Given the source rate in the same region of the ^{54}Mn spectrum is $\approx 8 \times 10^3$ cps. The error generated by the convolution process is order 2×10^{-6} which can be neglected in this analysis.

After energy scaling, and convergence, the pileup spectrum is subtracted from the starting spectrum generating the true ^{54}Mn pile-up corrected spectrum.

D. ROI of ^{54}Mn spectrum

The daily decay rate from the ^{54}Mn-corrected spectrum can be determined using differing techniques. One technique is to fit the photopeak shape. The drawback of this method is

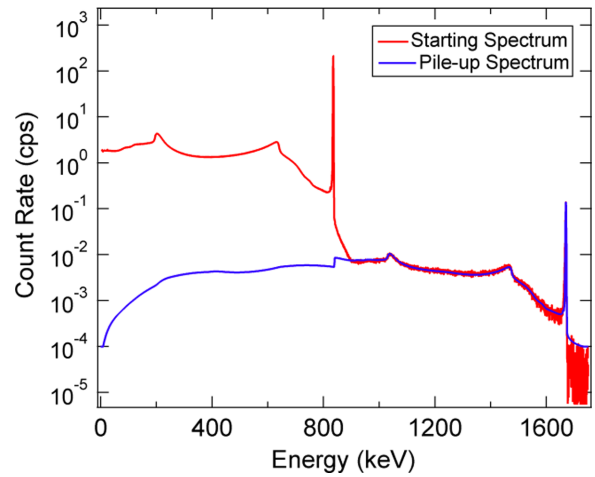

FIG. 10. Calculated ^{54}Mn pileup spectrum (blue) with the starting spectrum (red) demonstrating the fit achieved by the deconvolution algorithm.

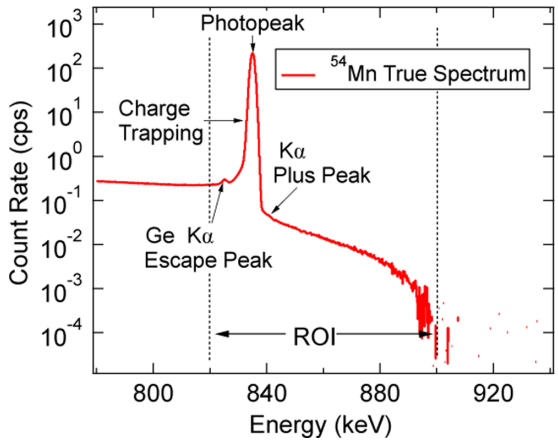

FIG. 11. The ROI, from 820 to 900 keV, is selected from the corrected daily ^{54}Mn spectrum.

that the photopeak is too complicated to model to the level of accuracy required. For example, charge trapping and trapped charge release occur in the HPGe detector during the γ-ray interaction process. These effects alter the HPGe line shape, as shown in Fig. 11, and may cause reduced or excess energy to be measured in the HPGe detector than is deposited by the γ ray. In this experiment the measured high-energy tailing extends as high as 60 keV away from the photopeak centroid. Such energy shifts associated with the photopeak have been discussed elsewhere [51–53] and reported to occur at the level of $\approx 10^{-3}$.

However, because of the very high precision required in this experiment, 10^{-5}, the high-energy tailing contribution, above the photopeak centroid, is well measured. While the high-energy tailing is correctly taken as part of the photopeak, there is a question of a similar feature effecting the lower-energy sideband that is used to correct the ROI region. To estimate the size of this effect in the lower sideband, the ROI tail is scaled to the sideband using the first day's spectrum, in which the effect is largest. The rate in the high-energy ROI photopeak tail is 3.5 cps. This is a factional rate of 2×10^{-3} when compared to the photopeak. The sideband region of equal energy width below the ROI has a total rate of 0.1 cps, yielding an estimated higher-energy "tailing rate" from the sideband of 2×10^{-4} cps, which is not measurable in this experiment. For these reasons, the ROI has been selected to include the high-energy photopeak tailing. Note that after the background and pileup corrections, there are effectively zero events above the ROI energy band, which extends from 820 to 900 keV. In addition, the low-energy edge of the band has been selected to include "charge trapping" as well as the k_α escape peak in the Ge crystal. These escape events occur when a surface Ge atom radiates a k_α photon away from the crystal and, thus, its energy is lost. Likewise, the k_α pileup from the ^{54}Mn source and the photopeak have not been removed, because these are photopeak events, while energy shifted, they are not lost out of the ROI region, as shown in Fig. 11.

Thus, the ROI is a fixed-energy region instead of a fixed-channel range. Selecting a fixed-energy region is managed by using the time-dependent energy spectrum calibration coefficients.

TABLE XIII. The average individual error contributions in the ROI using the ^{54}Mn daily spectra.

Averaged correction per day in ROI	Count rate in ROI (cps)	Error rate in ROI (cps)
Statistical	1431.43	1.0×10^{-2}
Dead time (0.029 s/day)	1431.43	9.7×10^{-3}
ROI uncertainty (2.2×10^{-2} keV)	0.18	1.8×10^{-2}
Background reactor off	0.056	1.4×10^{-5}
Background reactor on	0.086	2.4×10^{-5}
Pile-up	1.70	3.4×10^{-5}
Total error rate (cps)		2.2×10^{-2}
Sensitivity $\delta R/R$		1.5×10^{-5}

Having selected the ROI, Table XIII provides a summary of the error for each 24-h data point, including the electronic dead-time correction, the background spectrum subtraction, the pile-up spectrum correction, statistical error from counting, and systematic error from the instruments. The total error per day is 0.022 cps. Averaging the daily measured decay rate in the ROI over the full length of the experiment yields on average count rate. Using this average, the per-day sensitivity is $\delta\lambda/\lambda \approx 1.5 \times 10^{-5}$.

XIII. ANALYSIS OF CORRECTED ^{54}Mn SPECTRA

The ^{54}Mn ROI daily decay rate as a function of time is shown in Fig. 12. The rate was calculated for each spectrum starting August 30, 2015, at 23:58:22, and ending March 09, 2016, at 23:12:51. The time period includes four reactor-off and four reactor-on periods. Those daily runs which cover the transition time of the reactor-on or reactor-off period have been removed to reduce possible error. The data collection consists of a continuous period including 87 reactor-on days and 105 reactor-off days over 192 days of data collection. The ROI count rate was initially 1754.31 ± 0.15 cps but decayed to approximately 1146.37 ± 0.12 cps at the end of the experiment. The data point for each day is plotted at the average

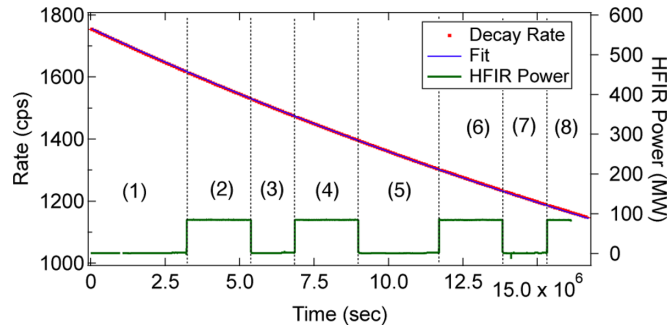

FIG. 12. Daily ^{54}Mn ROI (between 820 to 900 keV) decay rate and fit. Error bars are too small to be shown. The HFIR reactor power is also shown. The Periods 1:(37 days), 3:(16 days), 5:(31 days), and 7:(16 days) are the reactor-off periods. The Periods 2:(24 days), 4:(24 days), 6:(23 days), and 8:(16 days) are reactor-on periods.

TABLE XIV. Comparison of the in-phase and out-of-phase ROI oscillation with the calibration b term and the humidity (inside the HFIR complex) oscillations.

ROI oscillation	Phase (ϕ)	In phase	Phase (ϕ)
In phase	-111 ± 0.5 day	b_r terms	-122 ± 2 day
Out of phase	71 ± 0.5 day	Humidity	79 ± 1 day

time weighed by an exponential function calculated using the standard ^{54}Mn mean lifetime τ (450.41±0.29 days) [48].

The analysis of the decay rate requires correction for the effect of environmental influences, as measured and discussed concerning the calibration b term and c term. To correct for the b term the decay function includes a single periodic function with a phase to take into account the known yearly environmental oscillations observed in the data,

$$R(t) = ae^{-t/\tau} + A\sin(\omega t + \phi). \tag{26}$$

Again, τ is fixed at the mean lifetime of ^{54}Mn [48], ω is the periodicity, fixed at one year, and ϕ is the phase relative to the start of the experiment. Including the yearly environmental effects in the fit reduces the χ^2 per degree of freedom from ≈100 to 1.54, using four degrees of freedom. As shown in Table XIV the the oscillation has a good match to the b_r parameter oscillation and has a good out-of-phase match to the humidity. This is as expected if the oscillation is driven by the yearly variations in the humidity acting on the X-cooler. The amplitude of the oscillation is 1.55 ± 0.01 cps. When compared to the average rate in the ROI, 1431.43 ± 0.18 cps, the fractional effect is at the level of 1.1×10^{-3}.

The fitting function, Eq. (26), successfully removes the oscillation behavior. The minimum value occurs on September 20, 2015, which is nearly 21 days from the starting date, August 30, 2015. This date is not associated with the Earth's perihelion or the aphelion, which occurred January 2, 2016, at 17:49 (EST), and July 6, 2015, at 14:40 (EST) [54], as shown in Fig. 13. If the periodicity is allowed to vary, then the χ^2/DoF is unchanged and yields an oscillation of 363.6 days, in agreement within error with the 1-year fixed value. Therefore, the oscillation of the decay rate does not correlate to the solar neutrino flux variation due to the Earth's motion.

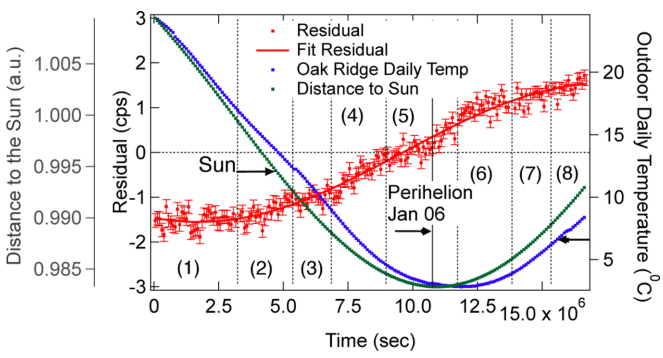

FIG. 13. The oscillation term (red points) found by subtraction of only the exponential term from the data [Eq. (26)] and its fit (red line). Also shown for comparison, (right axis, blue line) the daily outdoor temperature and (far left axis, green line) the Earth's distance from the Sun. Neither is in phase with the environmental oscillations inside the HFIR complex. The experimental periods are indicated.

As an aside, the subtraction of this low-frequency term in no way affects the sensitivity of the search for decay rate parameter variations in this experiment but instead demonstrates the ability to reject environmental effects, as the HFIR characteristic on-time period is 30 days a much higher frequency than the 1-year environmental frequency being filtered out in this search.

XIV. SIDEBAND NONLINEAR ENERGY CALIBRATION CORRECTIONS DUE TO ENVIRONMENTAL EFFECTS

As with the linear calibration term, because the DEPEC-50 spectrometer electronics and the X-cooler are located outside the controlled environmental housing, environmental factors such as temperature, pressure, and humidity cause variations in the nonlinear energy scale calibration parameter, c_r. The use of nonlinear calibrations has previously been presented for both the source and background spectra. The nonlinear energy scale correction is given in Eq. (21) and repeated here for clarity,

$$E = a_r + b_r x + c_r x^2. \tag{27}$$

Again, a_r, b_r, and c_r are the calibration coefficients of the rth daily spectrum and x is the channel number of the spectrum. The ROI data are analyzed using the cps in a fixed-energy band ΔE which includes the photopeak. For illustration, using a band containing n fixed bins, this band is given by

$$\begin{aligned}\Delta E &= b_r(x_{i+n} - x_i) + c_r\left(x_{i+n}^2 - x_i^2\right) \\ &= [b_r + c_r(x_{i+n} + x_i)] \times (x_{i+n} - x_i).\end{aligned} \tag{28}$$

The error in the bands energy width generates an error in the counts associated with that band. The error in the width is

$$\delta(\Delta E) = [\delta b_r + \delta c_r(x_{i+n} + x_i)] \times (x_{i+n} - x_i). \tag{29}$$

b_r is well measured to a fractional accuracy of 7×10^{-5}, as shown in Fig. 6, and $c_r(\approx 10^{-8})$ is measured to a fractional accuracy of order 10^{-1}. Nonetheless, it is sensitive to environmental effects. At low bin number the nonlinear term has no effect on the energy bandwidth. However, as the bin number increases, and in the ROI band where $x_i \approx 4000$, the error in the bandwidth is dominated by the nonlinear term,

$$(\delta c_r \cdot 2x_i)^2 \geqslant (\delta b_r)^2, \tag{30}$$

so that the error on the width is given approximately by

$$\delta(\Delta E) \approx \delta c_r\left(x_{i+n}^2 - x_i^2\right). \tag{31}$$

The knowledge of c_r-term motion as a function of the environmental parameters can be found by study of the sideband residuals.

These expectations concerning δc_r are verified in the spectral data by study of the energy regions below the ROI. Regions were selected staring from 300 to 380 keV, 380 to 460 keV, 460 to 540 keV, 540 to 640 keV, as well as 640 to 820 keV all below the ROI. The daily decay rate for each of these energy regions is fit to the same function as the ROI using

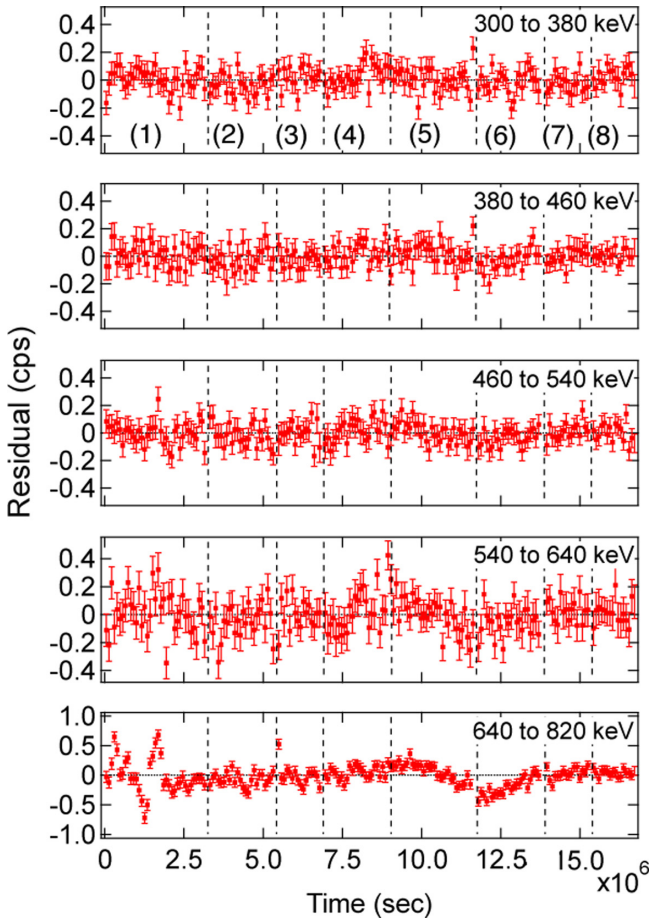

FIG. 14. Residuals for energy regions below the ROI from the corrected ^{54}Mn spectrum using Eq. (26). The residuals show the environmental effects strongly correlate with the increasing strength of the nonlinear term $c_r x^2$. Bandwidth in keV (from the top): (300,380), (380,460), (460,540), (540,640), and (640,820).

Eq. (26) and the residuals are displayed in Fig. 14. Again, only a and A are variables in the fit; ω, τ, and ϕ are the same coefficients used for the ROI. Figure 14 shows the residual for each energy regions, and Table XV gives the χ^2 per degree of freedom for each energy region.

As expected, the χ^2 per degree of freedom for the lower-energy bands is $\approx$1. However, because the c_r term has a significant effect only at high bin numbers, the χ^2 per DoF increases in the sideband region just below the photopeak to $\approx$12, due to the influence of environmental effects.

TABLE XV. The χ^2 per degree of freedom after fitting with Eq. (26) in Fig. 14.

Energy Region (keV)	χ^2 per degree of freedom
300 to 380	0.98
380 to 460	0.86
460 to 540	0.87
540 to 640	1.24
640 to 820	12.02

The environmental effects on c_r are significant, causing an incorrect assignment of the energy width of the ROI. An incorrect energy width causes motion of events from one band to another to be lost or gained as a function of the environmental changes. The motion of events is measured by the difference in the error in the energy width of the edge bins of the energy region. These effects can be calculated from

$$R_L \times f(E_L) - R_U \times f(E_U) = \delta R, \tag{32}$$

where $f(E_L)$ and $f(E_U)$ are the fractional variation in the edge bins of the sideband at the lower and upper edges. R_L, and R_U are the rates in the sideband edge channels of the spectrum. δR is the residual rate in that energy band. Because events enter or leave the band only through the edges, environmental effects on c_r can be corrected for by relating c_r to the residuals caused by the environmental factors. Equation (32) can be rewritten as

$$R_L \frac{\delta c_r \times x_L^2}{\Delta_{\rm bin}(E_L)} - R_U \frac{\delta c_r \times x_U^2}{\Delta_{\rm bin}(E_U)} = \delta R, \tag{33}$$

where δc_r is the correction to c_r found using the sideband residuals where the residuals are dominated by δc_r; $\delta c_r \times x^2$ is the small energy shift due to environmental factors. $\Delta_{\rm bin}(E)$ is the bin energy width at E. This correction provides a unique way to correct small electronic effects due to environmental factors.

Once the corrections are found to the nonlinear calibration term using the sideband, this improved knowledge is used to correct the ROI band. In order to find the correction in the ROI, the same energy width band has been selected starting from 740 to 820 keV which is the lower sideband of the ROI. The upper edge of this energy region connects to the lower edge of the ROI.

Before the environmental δc_r corrections can be found, the false decay term they induce must be subtracted from the sideband. The residuals of the ROI lower sideband are shown in Fig. 15. To correct for this, an exponential decay function, used only on this sideband region, is fit to the residuals,

$$\delta R(t) = C + D \times \exp(-t/\tau_1), \tag{34}$$

where C, D, and τ_1 are the fitting coefficients of this function. Once fit, the residuals in the energy region 740 to 820 keV drop the χ^2 per DoF from 12 to 1.49. τ_1 is found to have low frequency, 139 days, showing that this correction is not related to reactor operations, having a characteristic frequency of $\approx$30 days.

After removing the lower sideband false decay from the residuals, Fig. 16 makes clear the strong correlation between the remaining daily residual with temperature and humidity variations. The red squares in Fig. 16 (upper) include all sideband residual data points. The blue triangles only include the end of Periods 5 to 7 which is related to a significant drop in temperature due to an HVAC outage in the HFIR building, effecting only the equipment outside the shielding house. It is clear there are $\pm$0.6 cps variations with temperature deviations of -4 to 8 °C. Two linear fittings have been applied to the data set independently. The fitting coefficients from

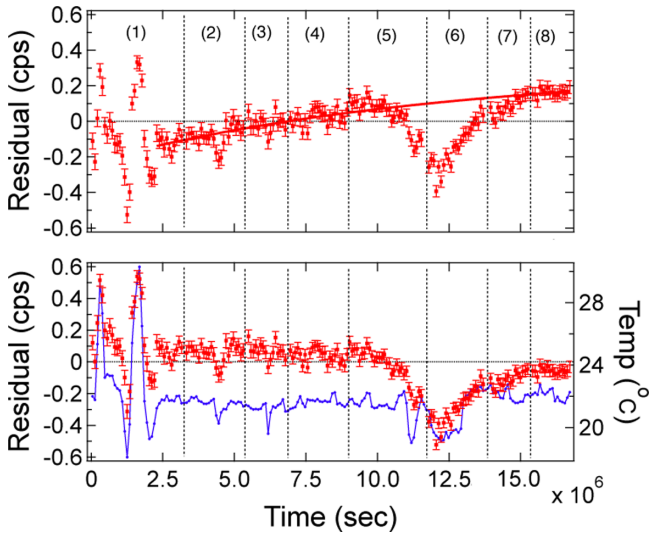

FIG. 15. Upper: Daily residuals of the sideband energy region (740 to 820 keV) in the ^{54}Mn spectra with false decay term fit [Eq. (34)]. Lower: Daily residuals (red) for the sideband energy region after subtraction of the false decay term fit. Significant fluctuations appear in Periods 1, 5, and 6, due to HVAC outages within the HFIR building. Ambient temperature (blue right axis) within the HFIR complex.

the red data point are different compared with the blue data points. The residual variations with temperature prove that environmental effects are causing the motion. However, the length of the time-dependent temperature variations also plays a role causing the difference between the red and blue data points. Because the variations of blue data points include both reactor-off and reactor-on periods, they are not caused by the reactor status. That is, antineutrino exposure is not the reason for this effect.

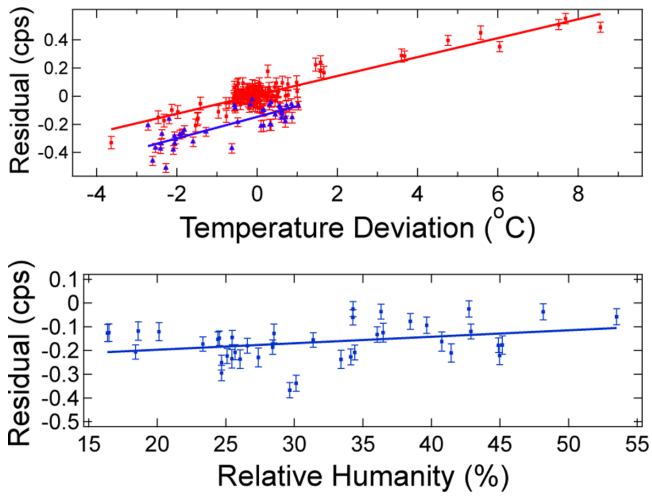

FIG. 16. Upper: Daily residuals and fits of the sideband energy region (740 to 820 keV) as a function daily average temperature (red) without Periods 5, 6, and 7 and separately (blue) Periods 5, 6, and 7. Lower: Daily residuals and fit of the sideband energy region as a function of daily relative humidity during periods having near zero temperature variations.

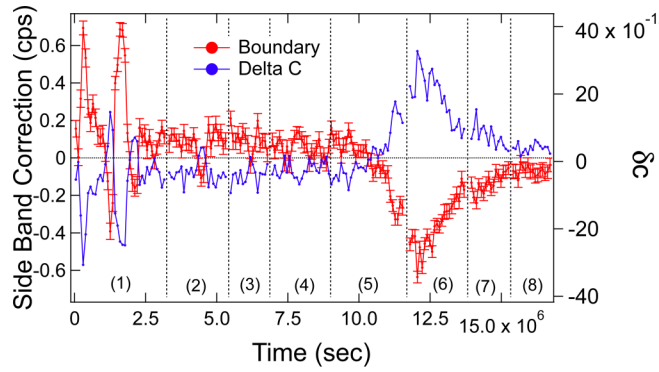

FIG. 17. Daily δc_r (blue right axis), found using Eq. (33) compared to the exponential function corrected residuals (red) for the sideband region 740 to 820 keV of the ^{54}Mn spectra.

Likewise, the residuals motion is correlated with humidity, as shown in Fig. 16 (lower), decoupled from the temperature variations by using only those data periods having near zero temperature deviation. It should be noted that the residual shifts displayed in Fig. 15 do not coincide with reactor-on and reactor-off cycles. Because of the strong correlation of the sideband residuals with environmental factors, these residual shifts are taken as environmental, to be used to correct for environmental factors in the ROI. That is, after the false decay subtraction, the remaining residuals from the lower sideband, having an energy bandwidth equal to the ROI region, are set to zero as a measure of the environmental factors. This preassumes that no measurable antineutrino effects are measurable in the sideband. This is reasonable as the data rate ratios between the sideband $\approx$0.1 cps compared to the photopeak ROI of 1800 cps is 5.6×10^{-5}. To further this point, if the size of the positive effect is $\approx 10^{-3}$ [5,22], as reported, then sensitivity required of the sideband compared to that of the photopeak is below the level of $\approx 10^{-7}$, which is not measurable in this experiment.

It is noted that the lower edge of the ROI is the same as the upper edge of the sideband. The upper edge of the ROI is zero after the pile-up correction. After using Eq. (33) to find δc from the sideband, shown in Fig. 17, the corrected daily decay rate for the ROI is then

$$\delta R_{\mathrm{ROI}} = R_{U(\mathrm{sideband})} \frac{\delta c_r \times x^2_{U(\mathrm{sideband})}}{\Delta_{\mathrm{bin}}[E_{U(\mathrm{sideband})}]}, \tag{35}$$

where $R_{U(\mathrm{sideband})} = R_{L(\mathrm{ROI})}$ and $x^2_{\mathrm{sideband}} = x^2_{\mathrm{ROI}}$. Note the sign changes for the correction. The rate from the upper sideband edge is the lower edge of the ROI. This occurs because events lost from one band edge is a gain to the other band, yielding

$$R_{\mathrm{Corrected\,ROI}}(t) = R_{\mathrm{ROI}}(t) + \delta R_{\mathrm{ROI}}. \tag{36}$$

To conclude this section, it must be emphasized that the false exponential was not used to correct the ROI or sideband data sets in any way.

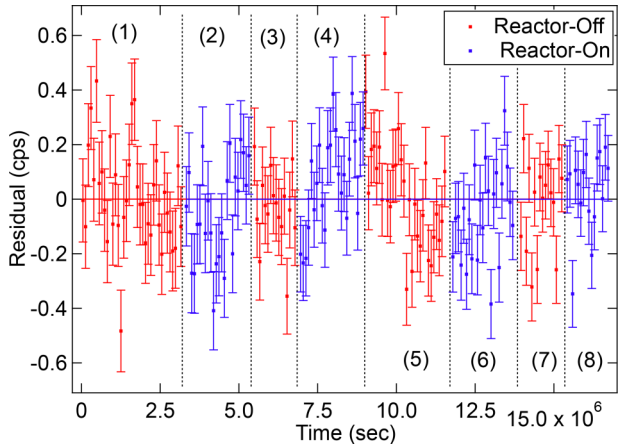

FIG. 18. Corrected ^{54}Mn ROI residuals as a function of time. The red data points indicate the residuals in reactor-off periods (1, 3, 5, and 7), and blue data points indicate the residuals in reactor-on periods (2, 4, 6, and 8).

XV. ^{54}Mn RESULTS AFTER ALL CORRECTIONS (ROI)

The corrected daily decay rate from the ^{54}Mn ROI was used to search for antineutrino interactions through decay parameter variations. The corrections made to the ROI rate are (1) the background subtraction correction, (2) the pile-up correction, (3) the fixed exponential fit subtraction, (4) a fixed periodic fit subtraction [Eq. (26)], and (5) a sideband environmental correction. Figure 18 shows the final residuals for the ROI as a function of time and reactor status. The red data points indicate the residuals in reactor-off periods, and blue data points indicate the residuals in reactor-on periods. Three different methods were used to search for an effect and estimate sensitivity, including (1) a simple average of the residual form each period without regard to reactor status, (2) segment analysis by checking three consecutive reactor cycles, and (3) step search, by comparing all reactor-on residuals to all reactor-off residuals.

A simple first test of the data is to average all residuals from each reactor-on and reactor-off period. This average analysis tests the consistency with the flatness of the residuals. Table XVI shows the average residual of each period yielding the size of its motion away from zero, δR (cps). Averaging all the periods without regard to reactor status yields $\delta R = (0.52 \pm 1.08) \times 10^{-2}$ cps and $\delta R/R = (3.62 \pm 7.53) \times 10^{-6}$ where R is taken as the experimental average rate. This test shows the residuals are consistent with an origin having a single value, zero, indicating no effect during the antineutrino exposure.

A second method is the walking window technique, taking advantage of the alternating reactor cycle pattern for the antineutrino flux. The two like reactor status periods are averaged into a single data point and compared to the average of the opposite reactor status they guard. The result is $\delta R = (2.11 \pm 2.13) \times 10^{-2}$ cps and $\delta\lambda/\lambda = (1.48 \pm 1.49) \times 10^{-5}$. The results are within one standard deviation and again consistent with no effect during the antineutrino exposure.

The strongest test of the data is to combine all the reactor-on data and compare to all the reactor-off data in search of a step. This method yields $\delta R = (4.83 \times 10^{-4} \pm 1.98 \times 10^{-2})$ cps and $\delta\lambda/\lambda = (0.034 \times 10^{-7} \pm 1.38 \times 10^{-5})$.

Because the walking window method creates correlations and does not use all the periods with equal strength, the limits are set using the combined technique and are shown in Table XVII.

TABLE XVI. Average residuals and uncertainty of each reactor-on and reactor-off period. The average of all residuals without regards to reactor status. The mean of all the data is less than one standard deviation away from zero. This test shows data consistency indicating no effect during the antineutrino exposure. R is taken as the experimental average ROI rate.

Period	Reactor status	Residual (cps)	Uncertainty (cps)
1	Off	9.35×10^{-3}	3.02×10^{-2}
2	On	-5.01×10^{-2}	3.07×10^{-2}
3	Off	-3.24×10^{-2}	3.57×10^{-2}
4	On	7.52×10^{-2}	2.92×10^{-2}
5	Off	2.24×10^{-3}	2.48×10^{-2}
6	On	-5.81×10^{-2}	2.73×10^{-2}
7	Off	-1.90×10^{-2}	3.28×10^{-2}
8	On	3.41×10^{-2}	3.22×10^{-2}
Averaged δR (cps)		5.18×10^{-3}	1.08×10^{-2}
Average sensitivity $\delta R/R$		3.62×10^{-6}	7.53×10^{-6}

XVI. ^{137}Cs ANALYSIS

Once data collection was complete using the ^{54}Mn source it was exchanged for a 1-μCi ^{137}Cs disk source. Data collection commenced July 5, 2016, at 13:07:37 EST, when the enclosure and HPGe crystal returned to thermal equilibrium. Data collection concluded November 13, 2016, at 12:16:08. During this interval, HFIR was at full power for 51 days during two reactor on cycles with refueling outages spanning 77 days in aggregate. Again, data were collected in energy bins ≈0.225 keV in width over the energy region from ≈4 to ≈3.7 MeV. During a 24-hour data run approximately 6.2×10^8 counts were collected with an associated statistical uncertainty of four parts in 10^5.

TABLE XVII. Summary of ^{54}Mn decay rate measurements at HFIR. All reactor-on data compared to all reactor-off data.

Antineutrino Flux	$F_{\bar{\nu}} = 2.86 \times 10^{12}$ (s^{-1} cm^{-2})
Measured Variation	$\frac{\delta\lambda}{\lambda} = (0.034 \pm 1.38) \times 10^{-5}$
68% Upper limit Confidence level	$\frac{\delta\lambda}{\lambda} \leqslant 1.41 \times 10^{-5}$
Measured cross section	$\sigma = (0.031 \pm 1.24) \times 10^{-25}$ (cm^2)
Sensitivity 68% Upper limit Confidence level	$\sigma \leqslant 1.29 \times 10^{-25}$ (cm^2)

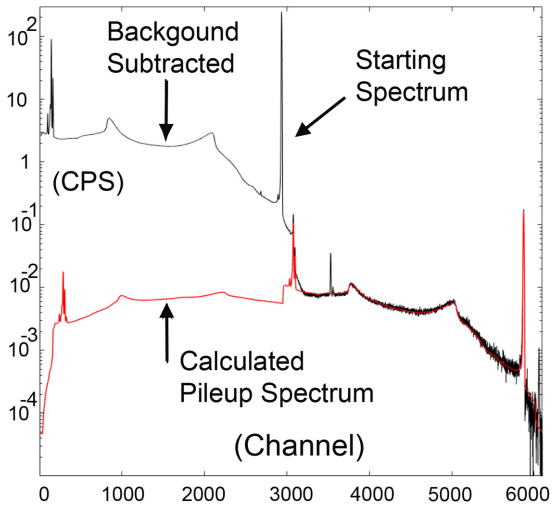

FIG. 19. ^{137}Cs pileup correction for the first daily run spectrum. Black: The background subtracted starting spectrum. Red: The pileup background to be subtracted.

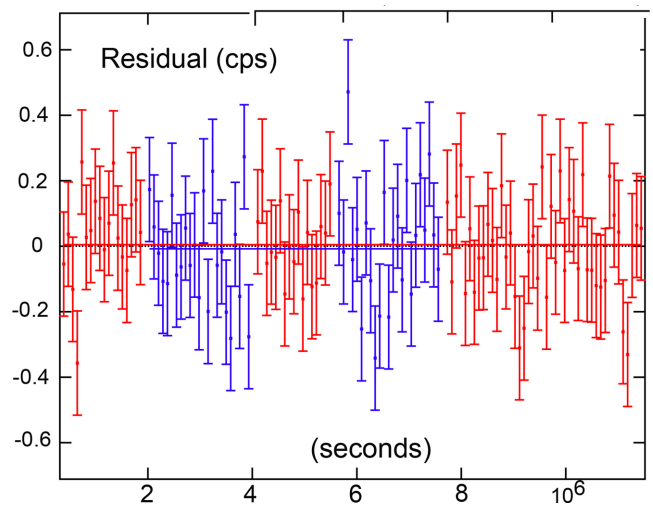

FIG. 20. ^{137}Cs ROI residuals as a function of time after corrections (1), (2), and (3). The red data points indicate the residuals in reactor-off periods, and blue data points indicate the residuals in reactor-on periods.

The ^{137}Cs photopeak is at 661.67 keV and has a 30.03 ± 0.09 year half-life. The ROI was selected to extend from 640 to 680 keV. During the course of the 128-day experiment the ROI count rate of the source ranged from 1.8996 to 1.8846 kHz. Both this longer half-life and lower-energy photopeak allowed the analysis of possible antineutrino effects on its decay to be considerably simpler in comparison to ^{54}Mn.

The corrections made to the ^{137}Cs ROI rate were the same extensively discussed in the analysis of the ^{54}Mn spectra. The corrections to the ^{137}Cs spectra included (1) the background subtraction correction: The background in the ROI was measured to be 0.064 ± 0.001 Hz when the reactor was on and 0.044 ± 0.001 Hz when the reactor was off. (2) The pile-up correction: The first daily correction is displayed in Fig. 19. The estimated remaining count rate, ≈0.035 Hz in each fully corrected spectrum, was estimated by extrapolation of the remaining counts in the pile-up region into the corrected region. This procedure gives a full spectrum pileup error of $\approx 5 \times 10^{-6}$. And (3) the fixed exponential fit subtraction: The residuals after corrections (1), (2), and (3) are displayed in Fig. 20 and, when comparing the reactor-on to reactor-off periods, yield a variation of $\delta\lambda/\lambda = (0.67 \pm 1.56) \times 10^{-5}$. The fourth correction used for the ^{54}Mn spectra, the fixed periodic fit subtraction, had little effect on the residuals, yielding the result $\delta\lambda/\lambda = (1.68 \pm 1.56) \times 10^{-5}$. However, unlike the ^{54}Mn fit using Eq. (26), when ω was unfixed the fit returned $\omega = 0$, that is, no oscillation. This is reasonable because of the shorter running period of the ^{137}Cs data collection in comparison to ^{54}Mn and because the ^{137}Cs running period was contained in a single season in which environmental parameters varied little. In addition, the fifth correction used for the ^{54}Mn spectra, the sideband environmental correction, was unnecessary for ^{137}Cs due to the lower energy of the ROI band. The motion caused by the nonlinear term, as shown in Fig. 14 and Table XV for ^{54}Mn, is, for ^{137}Cs, contained within the ROI band so has no effect on the residuals.

The 68% confidence upper limits for antineutrino interaction on ^{137}Cs, using corrections (1), (2), and (3), are displayed in Table XVIII.

XVII. CONCLUSION

The experiment has placed limits on decay rate parameter variation with sensitivity at 1 part of 10^5 by measuring the γ spectra from ^{54}Mn electron capture decay and ^{127}Cs β decay. The results place 68% confidence level upper limit on the cross section ranging from 0.1 barns to 0.005 barns [Eq. (16)], both of which are on the order of strong interaction cross sections.

Figure 21 compares the weak interaction decay data available in the literature as displayed in Tables VII and VIII and this experiment's final results in Tables XVII and XVIII. Each experiment is displayed by the logarithm ($\log_{10}$) of its cross section or sensitivity found using Eq. (16) as a function of the logarithm ($\log_{10}$) of the mean lifetime (seconds). All experiments are included regardless of reporting observed variation (triangles) or null observations (squares). The re-

TABLE XVIII. The 68% confidence upper limit on antineutrino interaction on ^{137}Cs. All reactor-on data compared to all reactor-off data.

Measured Variation	$\frac{\delta\lambda}{\lambda} = (0.67 \pm 1.56) \times 10^{-5}$
68% Upper limit Confidence level	$\frac{\delta\lambda}{\lambda} \leqslant 2.23 \times 10^{-5}$
Cross section Sensitivity	$\sigma = (1.71 \pm 3.98) \times 10^{-27}$ cm^2
68% Upper limit Confidence level	$\sigma \leqslant 5.69 \times 10^{-27}$ cm^2

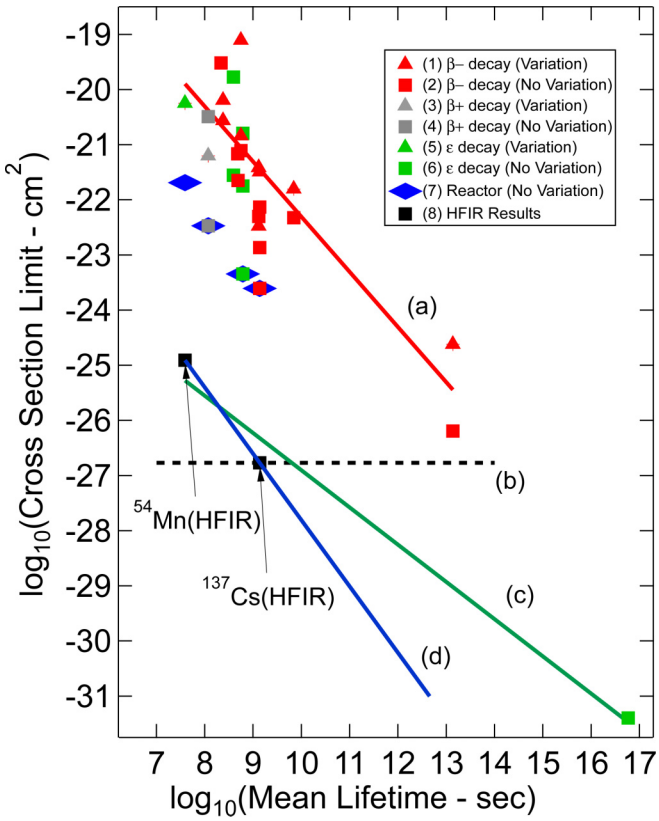

FIG. 21. The logarithmic ($\log_{10}$) cross-section sensitivity of those weak interaction decay experiments measuring time-dependent variations (triangles), no evidence of variation (squares), and this experiment's HFIR results, all as a function of the logarithm mean nuclear decay lifetime. The data are based on Table VII and VIII. The data include (1) β^- decay with variation results [1,3,6,15,17–20,24], (2) β^- decay with no effect results [8,27–29,31–33], (3) β^+ decay with variation results [7], (4) β^+ decay with no effect results [36], (5) electron capture decay with variation results [22], (6) electron capture decay with no effect results [8,32,33], (7) reactor antinuetrino as a test source with no effect results [30], and (8) the HFIR ^{54}Mn and ^{137}Cs results. See the text for explanation of the curves (a), (b), (c), and (d). The strong interaction α-decay result having a variation [5] and those with no variation [31,32,38] can be compared in Tables VII and VIII.

ported decay modes include (1) the negative β decay with time-dependent variation results (red triangles) [1,3,6,15,17–20,24], (2) the negative β decay with "null" variation results (red squares) [8,27–29,31–33], (3) the positive β decay with time-dependent variation results (gray triangles) [7], (4) the positive β decay with "null" variation results (gray squares) [36], (5) the electron capture β decay with time-dependent variation results (green triangles) [22], (6) the electron capture β decay with "null" variation results (green squares) [8,32,33], (7) the reactor antineutrino "null" variation results (blue squares) [30], and (8) this experiment's HFIR ^{54}Mn and ^{137}Cs results (black squares).

In this search the meaning of an excluded region is not well defined. However, it is expected that the cross-section sensitivities for neutrino and antineutrino interactions at a fixed measuring sensitivity should follow the curve

$$\sigma = A\,\tau^P, \tag{37}$$

where A and P are the fitting coefficients and τ is the isotopes mean lifetime. As a comparison, a fit is made to those experiments reporting decay rate parameter variations and displayed in Fig. 21 as curve (a) and in Table XIX. This experiment's null results lay $\approx 10^{-5}$ below this positive variations line.

TABLE XIX. Fit coefficients from the four curves displayed Fig. 21 found using Eq. (37).

Curve	A	P
(a) Observed variation	−12.31	−1
(b) Cross-section-only comparison	−24.87	0
(c) Exclusion region	−19.54	−0.71
(d) This experiment lifetime exclusion	−17.28	−1

Another approach is to assume that the cross section is the fundamental. In this case, curve (b) compares this experiment's ^{137}Cs limit, its most sensitive cross-section limit, to all experiments. This experiment is more sensitive than all previous experiments reporting positive ^{137}Cs decay rate parameter variations by a factor of 10^4 and is in disagreement with the most sensitive positive result experiment on this basis by a factor of 10^2.

A third approach is to use use the most sensitive null experiments as input to Eq. (37). The result is curve (c) in Fig. 21 and in Table XIX, a fit of this experiment's two results and a null solar neutrino-based experiment using ^{40}K [33]. The connection between these two independent experiments results maps out an exclusion zone in the cross section versus nuclear mean lifetime space excluding decay rate parameter variations, again at a level 10^4 times more sensitive than any previously reported positive result.

Finally, curve (d) displays the exclusion zone if extrapolated using only this experiment's two results and again is in disagreement with all positive result experiments.

The properties of these exclusion curves, as displayed in Fig. 21 and in Table XIX, make a convincing case that those measurements reporting decay rate parameter variations are not consistent with the source of the variations being caused by neutrino or antineutrino interactions.

ACKNOWLEDGMENTS

The authors thank the HIFR staff for their operational support at Oak Ridge National Laboratory, necessary to accomplish the experiment. Special thanks is given to John Herczeg, Nuclear Science Division of the Department of Energy, for his support, encouragement, and interest in seeing this experiment to completion. Thanks to Advanced Physics Technologies for production of the neutron shielding and its expertise with HPGe detectors. This work was funded under a grant from the U.S. Department of Energy Office of Nuclear Energy, Contract No. DE-DT0004091.

[1] D. E. Alburger, G. Harbottle, and E. F. Norton, Half-life of ^{32}Si, Earth Planet. Sci. Lett. **78**, 168 (1986).

[2] E. D. Falkenberg, Radioactive decay caused by neutrinos? Apeiron **8**, 32 (2001).

[3] E. D. Falkenberg, Reply to "Does radioactivity correlate with the annual orbit of earth around sun?" by G. W. Bruhn, Apeiron **9**, 41 (2002).

[4] J. H. Jenkins, E. Fischbach, D. J. II, R. H. Lee, and P. A. Sturrock, Concerning the time dependence of the decay rate of ^{137}Cs, Appl. Radiat. Isot. **74**, 50 (2013).

[5] J. H. Jenkins, E. Fischbach, J. B. Buncher, J. T. Gruenwald, D. E. Krause, and J. J. Mattes, Evidence of correlations between nuclear decay rates and earth–sun distance, Astropart. Phys. **32**, 42 (2009).

[6] J. H. Jenkins, K. R. Herminghuysen, T. E. Blue, E. Fischbach, D. J. II, A. C. Kauffman, D. W. Mundy, P. A. Sturrock, and J. W. Talnagi, Additional experimental evidence for a solar influence on nuclear decay rates, Astropart. Phys. **37**, 81 (2012).

[7] D. O'Keefe II, B. L. Morreale, R. H. Lee, J. B. Buncher, J. H. Jenkins, E. Fischbach, T. Gruenwald, D. Javorsek, and P. A. Sturrock, Spectral content of ^{22}Na/^{44}Ti decay data: Implications for a solar influence, Astrophys. Space Sci. **344**, 297 (2013).

[8] H. Schrader, Half-life measurements of long-lived radionuclides–new data analysis and systematic effects, Appl. Radiat. Isot. **68**, 1583 (2010).

[9] H. Schrader, Seasonal variations of decay rate measurement data and their interpretation, Appl. Radiat. Isot. **114**, 202 (2016).

[10] S. E. Shnoll, V. A. Kolombet, E. V. Pozharskii, T. A. Zenchenko, I. M. Zvereva, and A. A. Konradov, Realization of discrete states during fluctuations in macroscopic processes, Phys. Usp. **41**, 1025 (1998).

[11] S. E. Shnoll, T. A. Zenchenko, K. I. Zenchenko, E. V. Pozharskii, V. A. Kolombet, and A. A. Konradov, Regular variation of the fine structure of statistical distributions as a consequence of cosmophysical agents, Phys. Usp. **43**, 205 (2000).

[12] P. A. Sturrock, E. Fischbach, and J. H. Jenkins, Further evidence suggestive of a solar influence on nuclear decay rates, Sol. Phys. **272**, 1 (2011).

[13] P. A. Sturrock, L. Bertello, E. Fischbach, D. J. II, J. H. Jenkins, A. Kosovichev, and A. G. Parkhomov, An analysis of apparent r-mode oscillations in solar activity, the solar diameter, the solar neutrino flux, and nuclear decay rates, with implications concerning the sun's internal structure and rotation, and neutrino processes, Astropart. Phys. **42**, 62 (2013).

[14] P. A. Sturrock, E. Fischbach, D. J. II, J. H. Jenkins, R. H. Lee, J. Nistor, and J. D. Scargle, Comparative study of beta-decay data for eight nuclides measured at the physikalisch-technische bundesanstalt, Astropart. Phys. **59**, 47 (2014).

[15] P. A. Sturrock, A. G. Parkhomov, E. Fischbach, and J. H. Jenkins, Power spectrum analysis of {LMSU} (lomonosov moscow state university) nuclear decay-rate data: Further indication of r-mode oscillations in an inner solar tachocline, Astropart. Phys. **35**, 755 (2012).

[16] P. A. Sturrock, G. Steinitz, E. Fischbach, D. J. II, and J. H. Jenkins, Analysis of gamma radiation from a radon source: Indications of a solar influence, Astropart. Phys. **36**, 18 (2012).

[17] P. A. Sturrock, G. Steinitz, E. Fischbach, A. Parkhomov, and J. D. Scargle, Analysis of beta-decay data acquired at the physikalisch-technische bundesanstalt: Evidence of a solar influence, Astropart. Phys. **84**, 8 (2016).

[18] A. G. Parkhomov, Bursts of count rate of beta-radioactive sources during long-term measurements, Int. J. Pure Appl. Phys. **1**, 119 (2005).

[19] Yu. A. Baurov, Yu. G. Sobolev, Yu. V. Ryabov, and V. F. Kushniruk, Experimental investigations of changes in the rate of beta decay of radioactive elements, Phys. At. Nucl. **70**, 1825 (2007).

[20] A. Parkhomov, Deviations from beta radioactivity exponential drop, J. Mod. Phys. **2**, 1310 (2011).

[21] E. Fischbach, J. B. Buncher, J. T. Gruenwald, J. H. Jenkins, D. E. Krause, J. J. Mattes, and J. R. Newport, Time-dependent nuclear decay parameters: New evidence for new forces? Space Sci. Rev. **145**, 285 (2009).

[22] J. H. Jenkins and E. Fischbach, Perturbation of nuclear decay rates during the solar flare of 2006 december 13, Astropart. Phys. **31**, 407 (2009).

[23] D. E. Krause, B. A. Rogers, E. Fischbach, J. B. Buncher, A. Ging, J. H. Jenkins, J. M. Longuski, N. Strange, and P. A. Sturrock, Searches for solar-influenced radioactive decay anomalies using spacecraft {RTGs}, Astropart. Phys. **36**, 51 (2012).

[24] D. P. Veprev and V. I. Muromtsev, Evidence of solar influence on the tritium decay rate, Astropart. Phys. **36**, 26 (2012).

[25] J. A. Formaggio and G. P. Zeller, From ev to eev: Neutrino cross sections across energy scales, Rev. Mod. Phys. **84**, 1307 (2012).

[26] K. S. Krane, *Introductory Nuclear Physics* (John Wiley & Sons, Inc., New York, 1988).

[27] G. W. Bruhn, Does radioactivity correlate with the annual orbit of earth around sun? Apeiron **9**, 28 (2002).

[28] K. Kossert and O. J. Nähle, Long-term measurements of ^{36}Cl to investigate potential solar influence on the decay rate, Astropart. Phys. **55**, 33 (2014).

[29] K. Kossert and O. J. Nähle, Disproof of solar influence on the decay rates of Y, Astropart. Phys. **69**, 18 (2015).

[30] R. J. de Meijer, M. Blaauw, and F. D. Smit, No evidence for antineutrinos significantly influencing exponential β^+ decay, Appl. Radiat. Isot. **69**, 320 (2011).

[31] T. M. Semkow, D. K. Haines, S. E. Beach, B. J. Kilpatrick, A. J. Khan, and K. O'Brien, Oscillations in radioactive exponential decay, Phys. Lett. B **675**, 415 (2009).

[32] H. Siegert, H. Schrader, and U. Schötzig, Half-life measurements of europium radionuclides and the long-term stability of detectors, Appl. Radiat. Isot. **49**, 1397 (1998).

[33] E. Bellotti, C. Broggini, G. D. Carlo, M. Laubenstein, and R. Menegazzo, Search for correlations between solar flares and decay rate of radioactive nuclei, Phys. Lett. B **720**, 116 (2013).

[34] E. Bellotti, C. Broggini, G. D. Carlo, M. Laubenstein, and R. Menegazzo, Search for time dependence of the ^{137}Cs decay constant, Phys. Lett. B **710**, 114 (2012).

[35] E. Bellotti, C. Broggini, G. D. Carlo, M. Laubenstein, and R. Menegazzo, Search for time modulations in the decay constant of ^{40}K and ^{226}Ra at the underground gran sasso laboratory, Phys. Lett. B **780**, 61 (2018).

[36] E. B. Norman, E. Browne, H. A. Shugart, T. H. Joshi, and R. B. Firestone, Evidence against correlations between nuclear decay rates and earth–sun distance, Astropart. Phys. **31**, 135 (2009).

[37] R. J. de Meijer and S. W. Steyn, Upper limit on the cross section for reactor antineutrinos changing ^{22}Na decay rates, arXiv:1409.6969.

[38] P. S. Cooper, Searching for modifications to the exponential radioactive decay law with the cassini spacecraft, Astropart. Phys. **31**, 267 (2009).

[39] A. Bellerive, Review of solar neutrino experiments, Int. J. Mod. Phys. A **19**, 1167 (2004).

[40] R. Davis, D. S. Harmer, and K. C. Hoffman, Search for Neutrinos from the Sun, Phys. Rev. Lett. **20**, 1205 (1968).

[41] P. Anselmann, W. Hampel, G. Heusser, J. Kiko, T. Kirsten, M. Laubenstein, E. Pernicka, S. Pezzoni, U. Rönn, M. Sann *et al.*, Gallex solar neutrino observations: Complete results for gallex ii, Phys. Lett. B **357**, 237 (1995).

[42] J. N. Abdurashitov, T. J. Bowles, M. L. Cherry, B. T. Cleveland, R. Davis, Jr., S. R. Elliott, V. N. Gavrin, S. V. Girin, V. V. Gorbachev, T. V. Ibragimova, A. V. Kalikhov, N. G. Khairnasov, T. V. Knodel, K. Lande, I. N. Mirmov, J. S. Nico, A. A. Shikhin, W. A. Teasdale, E. P. Veretenkin, V. M. Vermul, D. L. Wark, P. S. Wildenhain, J. F. Wilkerson, V. E. Yants, and G. T. Zatsepin (SAGE Collaboration), Measurement of the Solar Neutrino Capture Rate by Sage and Implications for Neutrino Oscillations in Vacuum, Phys. Rev. Lett. **83**, 4686 (1999).

[43] B. Aharmim, S. N. Ahmed, A. E. Anthony, N. Barros, E. W. Beier, A. Bellerive, B. Beltran, M. Bergevin, S. D. Biller, K. Boudjemline *et al.*, Combined analysis of all three phases of solar neutrino data from the sudbury neutrino observatory, Phys. Rev. C **88**, 025501 (2013).

[44] G. Bellini, J. Benziger, D. Bick, G. Bonfini, D. Bravo, M. B. Avanzini, B. Caccianiga, L. Cadonati, F. Calaprice, P. Cavalcante *et al.*, Final results of borexino phase-i on low-energy solar neutrino spectroscopy, Phys. Rev. D **89**, 112007 (2014).

[45] G. Kessler, *Proliferation-Proof Uranium / Plutonium Fuel Cycles Safeguards and Non-Proliferation* (KIT Scientific, Karlsruhe, Germany, 2011).

[46] J. Heim, J. Nistor, and D. Koltick, Extended stability of HPGe spectrometer with environmental control at the high flux isotope reactor, Phys. Proc. **90**, 429 (2017).

[47] Y. P. Varshni, Temperature dependence of the energy gap in semiconductors, Physica **34**, 149 (1967).

[48] National Nuclear Data Center, Brookhaven National Laboratory (2021), http://www.nndc.bnl.gov/chart/.

[49] S.-C. Liu, *Test of Decay Rate Parameter Variation Due to Anti-neutrino Interactions* (Internet Archive, San Fransisco, CA, 2019).

[50] D. York, N. M. Evensen, M. L. Martinez, and J. De Basabe Delgado, Unified equations for the slope, intercept, and standard errors of the best straight line, Am. J. Phys. **72**, 367 (2004).

[51] R. A. Meyer, K. G. Tirsell, and G. A. Armantrout, Current research relevant to the improvement of γ-ray spectroscopy as an analytical tool, in *Proceedings of ERDA Symposium on x- and gamma-ray sources and applications held in Ann Arbor Michigan, May 19–21, 1976* (Scitech Connect, Washington, DC, 1976).

[52] M. Dojo, A shape function of photopeaks for gamma-ray spectrum analysis with ge (li) detectors, Nucl. Instrum. Methods **115**, 425 (1974).

[53] L. C. Longoria, A. H. Naboulsi, P. W. Gray, and T. D. MacMahon, Analytical peak fitting for gamma-ray spectrum analysis with ge detectors, Nucl. Instrum. Methods A **299**, 308 (1990).

[54] Astronomical Applications Department, The United States Naval Observatory, http://aa.usno.navy.mil/data/docs/EarthSeasons.php.